Integral-equation approach to resonances in circular two-layer flows around an island with bottom topography

Michael Rabinovich[1]†

[1]Department of Physics, Bar Ilan University, Ramat-Gan 52900, Israel

(Received xx; revised xx; accepted xx)

An integral-equation approach to the linear instability problem of two-layer quasi-geostrophic flows around a circular island with bottom topography is studied. The study extends an earlier barotropic model of similar geometry and topography and focuses on the degree to which the topographic waves in the lower layer resonate with the basic flow in each layer. The integral approach poses the instability problem in a physically elucidating way, in which the resonating neutral waves in the system can be identified directly. The flows investigated are composed of uniform potential-vorticity (PV) ring in each layer, having opposite signs. Four types of instabilities are identified: instability caused by the resonance of the Rossby waves traveling along the liquid contours at the edge of each PV ring (CC resonance), instability caused by the resonance of the wave at the upper-layer contour and the topographic waves outside the lower-layer contour (C_1T), a similar resonance of the lower layer contour with the topographic waves (C_2T), and a resonance between one of eigenmodes of the contours subsystem with the topographic waves (CCT). The three last resonances lead to a critical level instabilities, and can be identified as resonance of the contours' waves with a collection of singular topographic modes having a critical layer. The C_1T (C_2T) instability occurs when the lower-layer ring is thin enough and the basic flow travels counterclockwise (clockwise). The neutral PV perturbations in the outer region asymptotically behave as barotropic (BT) or baroclinic (BC) modes that, when traveling clockwise, have spiral shape and are wavelike in the radial direction. Usually the BT mode is the one that resonates with the contours, but in case of small growth rates the BC mode may be the dominant one. The nonlinear evolution of the CC resonance usually leads to emission of dipolar modons which then return to the island and re-emitted in a quasi-periodic manner. The contours-topography instabilities may produce a narrow PV ring at the lower layer at the location of the critical layers of the dominant resonating topographic perturbations; this ring interacts with the original rings to form a quasi-stationary structure (e.g. a tripole) that rotates counterclockwise for a relatively long time before splitting to emitted modons.

1. Introduction

Islands in the stratified ocean might have complex and variable current circulation patterns around them (Chopra 1973). Closed flows which are anomalous, i.e. follow an opposite direction to the overall circulation of the surrounding ocean, have been observed around Iceland, Taiwan, the islands of Kuril Chain (Shtokman 1966) and the Pribilof islands (Kowalik & Stabeno 1999). In most cases, these anomalous circulations are anticyclonic (clockwise) in the northern hemisphere and are wind-driven. Waves

---

† Email address for correspondence: michael.rabinovich@biu.ac.il

generated in the vicinity of the islands may be trapped by the slopping topography or the coast, and also contribute to the circulation strength; the trapping by islands was shown for barotropic flows (e.g. Longuet-Higgins 1967, 1969; Brink 1999) as well as for the stratified sea (e.g. Wunsch 1972; Dyke 2005; Mihanović *et al.* 2014). In this paper we study the conditions for instability of such baroclinic flows in an idealized model, where the island is circular and the bottom topography is conical (the beta cone model).

To account for the stratification of the ocean we use the two-layer quasi-geostrophic (QG) simplified model (Pedlosky 1964). The linear baroclinic instability problem was solved for the case of two-layer zonal uniform QG flow over a flat bottom by Phillips (1951), and later solved with including bottom topography by Mechoso (1980). For circularly symmetric flows, the instability problem was investigated by Flierl (1988) for baroclinic QG vortices with flat bottom and continuous stratification. Circular baroclinic two-layer flows were investigated by Solodoch *et al.* (2016), for flows confined to an annular channel; our model is different in several aspects. First, in our model there is no external boundary. Second, the basic flow is different as described below; especially, in our model the currents in the two layers may be opposite in direction. Related to this is the fact that in our case the ratio of the bottom slope to the basic isopycnal slope is not constant, and therefore this ratio plays no fundamental role.

The instability associated with idealized circularly-symmetric barotropic currents around circular islands with bottom topography was investigated by Rabinovich *et al.* (2018). There the flow was composed of two constants-PV rings around the island and the velocity outside the rings was zero. The purpose of this paper is to consider a variant of that model appropriate for a two-layer flow; now any layer consists of one constant-PV ring. The flows in the two layers may have opposite directions and the velocity outside the rings does not vanish identically, but rather only the barotropic velocity. figure 1 presents schematically the velocities and PVs profiles.

Physical interpretation of instabilities in two-layer shallow water flows is made possible using the concept of resonance. As has been shown by many authors, different types of instabilities can be identified as resonances between neutral waves; the type of the instability is determined by the interacting waves. The resonance is usually seen by the crossing of the dispersion curves, i.e. of the phase velocity vs. the wavenumber of the neutral modes (Cairns 1979). This was demonstrated in zonal shear flows (Satomura 1981; Kubokawa 1986; Hayashi & Young 1987) and zonal two-layer flows (Jones 1967; Sakai 1989; Iga 1997; Ribstein & Zeitlin 2013). In all these papers the resonant viewpoint was only applied to the case of shallow water systems without the QG approximation; in this paper it is applied also to QG flows.

To identify the resonances in a simple way, an integral-equation approach to the linear instability problem is undertaken. The integral approach was used so far only for barotropic flows by Kamp (1991), with no further development elsewhere to baroclinic flows; this paper fills this gap. It is shown that the integral approach poses the instability problem in a physically elucidating way, in which the coupling between the various wave types can be identified directly.

The basic flow considered in this paper is fundamentally different from the barotropic case studied by Rabinovich *et al.* (2019) since here outside the rings the basic velocity at the lower layer is nonzero, as well as the PV gradient (see figure 1). This fact makes possible the existence of singular neutral perturbations whose phase velocity is equal to the basic velocity at some place, i.e. having a critical layer (Lin 1945; Adam 1986). It is known that if linear stability analysis shows that critical-layer eigenfunctions are neutrally stable, more careful analysis of the initial-value problem shows that they actually cause an algebraic time dependence asymptotically with time (Case 1960; Briggs *et al.* 1970).

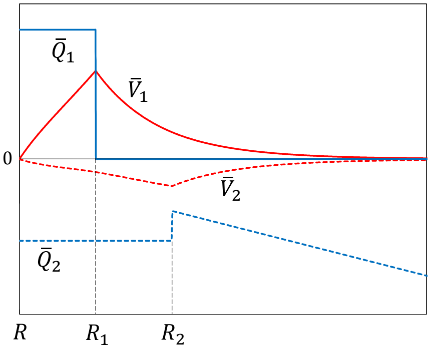

Figure 1: Schematic profiles of the basic velocity in the upper layer $\bar{V}_1$ (solid, red online), in the lower layer $\bar{V}_2$ (dashed, red online), the PV in the upper layer Q_1 (solid, blue online) and in the lower layer Q_2 (dashed, blue online).

The time dependence is found mathematically from the singularities of the modes on the complex frequency plane. Here on the beta cone it is shown that new singularities, not present in the zonal case, appear; their damping effect is analytically calculated.

Critical layer instability (Bretherton 1966) was observed experimentally by Riedinger *et al.* (2010) for columnar vortex in stratified fluid and studied in shallow water one-layer flows (Riedinger & Gilbert 2014). Iga (1999*a*) have shown that this instability can be interpreted as resonance of a nonsingular mode with a collection of singular modes. For the basic flow considered in this paper, resonances involving the topographic waves at the lower layer lead to a critical-layer instability. The resonating perturbations in this case are identified, and its effect on the nonlinear evolution of the flow is studied numerically.

The outline of this paper is as follows. In §2 we present the basic equations of the model of quasigeostrophic two-layer flows, and in §3 we derive the integral eigenvalue equation of the linear stability analysis. In §4 we apply the integral equation to the basic flow composed of two layer PV rings schematically plotted in figure 1. The resonance viewpoint is then presented for this flow in §5. In §6 the spectrum of solutions in the exterior region $r > R_2$ is discussed. These neutrally stable solutions (according to the linear stability analysis) are the ones that may resonate with the waves at the contours of the PV discontinuities at R_1 and R_2; their damping over time is also found. In §7 the resonances are further explored by the dispersion curves; the growth rates and the structure of the unstable perturbations are calculated, and the conditions for the dominance of barotropic vs. baroclinic couplings are discussed. In §8 the influence of the instability type on the nonlinear evolution of the flow is examined.

2. Two layer flows on a beta cone. Governing equations

Consider a two-layer quasigeostrophic (QG) model in which the flow surrounds a cylindrical island. The bottom outside the island is assumed to have a constant radial slope, so that the depth increases linearly offshore. Under the quasigeostrophic approximation and the rigid-lid condition at the sea surface, the flow is effectively two-dimensional in each layer. The variables of the upper and lower layers are denoted by the subscript 1 and 2, respectively. The unperturbed layer thickness is denoted by H_i (i=1,2), and their sum by H. In the polar coordinates r and θ, the radial and azimuthal components of the velocity, u_i and v_i respectively in each layer ($i = 1, 2$), can be expressed in terms of a streamfunction Ψ_i via the equations

$$u_i = -\frac{1}{r}\frac{\partial \Psi_i}{\partial \theta}, \quad v_i = \frac{\partial \Psi_i}{\partial r}. \tag{2.1}$$

In the following whenever the subscript i appears it refers to the i-th layer. The slope at the bottom introduces a linear term in r for the PV at the lower layer (see Rabinovich *et al.* (2018) for details). The proportionality constant is the topographic beta, $\beta = -f\tan(\alpha)/H_2$, where f is the Coriolis parameter. It is assumed that the island's size is small compared to the planetary scale, so f may be regarded as being constant (this is analogous to the f-plane approximation, cf. Pedlosky 2013). For an island in the northern hemisphere, β is negative.

In terms of the streamfunctions, the PVs in layers 1 and 2 are defined as (cf. Pedlosky 2013)

$$Q_1 = \nabla^2\Psi_1 - \frac{f^2}{g'H_1}(\Psi_1 - \Psi_2), \quad Q_2 = \nabla^2\Psi_2 + \frac{f^2}{g'H_2}(\Psi_1 - \Psi_2) + \beta r, \tag{2.2}$$

where $g' = g(\rho_2 - \rho_1)/\rho_1$ is the reduced gravity (g being the gravitational acceleration, ρ_1 and ρ_2 being the densities of the layers).

On the beta cone, a natural length scale is the radius of the island R. We are interested in flows whose horizontal length scale is R, such that the curvature plays a dominant role, so $r \sim R$. Flows having much smaller length scale behave locally as straight flows, while at much larger length scales the island's influence is negligible. In §3 the basic flow is defined, where the PV in the upper layer is constant inside a ring, $\mathit{\Gamma}_1$. This determines a scale for the time, $1/|\mathit{\Gamma}_1|$. Therefore, assuming that the time scales advectively, we tranform the variables to non-dimensional variables via

$$t \to t/|\mathit{\Gamma}_1|, \quad r \to Rr, \quad Q_i \to |\mathit{\Gamma}_1|Q_i, \quad \Psi_i \to |\mathit{\Gamma}_1|R^2\Psi_i, \quad \beta \to |\mathit{\Gamma}_1|\beta/R. \tag{2.3}$$

Non-dimensionalization of equations (2.2) then yields

$$Q_1 = \nabla^2\Psi_1 - \frac{\Lambda^2}{\lambda_1}(\Psi_1 - \Psi_2), \quad Q_2 = \nabla^2\Psi_2 + \frac{\Lambda^2}{\lambda_2}(\Psi_1 - \Psi_2) + \beta r, \tag{2.4}$$

where $\Lambda^2 = (R/L_{Ro})^2$ is the reverse Burger number, and $L_{Ro} = \sqrt{g'H/f_0^2}$ is the Rossby deformation radius. In the ocean, L_{Ro} varies from about 1km at high latitudes to about 400km at the equator (Houry *et al.* 1987). Small islands may have a radius of few kilometers, while large ones may reach a radius of 200km. Therefore Λ may change from 10^{-4} to 200. In order to be consistent with the quasigeostophic approximation mentioned above, Λ should be of order 1 or less (Pedlosky 2013). Therefore, mostly we use $\Lambda = 1$; This means, that the island's size is of the same order of magnitude as Rossby deformation radius. The relative thickness of each layer is denoted by $\lambda_i = H_i/H$ $(i = 1, 2)$, H being the total thickness of the fluid, $H = H_1 + H_2$.

The PV conservation equations governing the dynamics are

$$\frac{\partial Q_i}{\partial t} + \frac{1}{r}\left(\frac{\partial \Psi_i}{\partial r}\frac{\partial Q_i}{\partial \theta} - \frac{\partial \Psi_i}{\partial \theta}\frac{\partial Q_i}{\partial r}\right) = 0 \quad (i = 1, 2) \tag{2.5}$$

3. The integral eigenvalue equations

We represent the PVs $Q_{1,2}$ and the streamfunctions $\Psi_{1,2}$ of the flow as sums of the basic-state values (indicated by bar) and the perturbations,

$$Q_i = \bar{Q}_i(r) + q_i(r, \theta, t), \quad \Psi_i = \bar{\Psi}_i(r) + \psi_i(r, \theta, t). \tag{3.1}$$

Under the assumption of small perturbations, the linearized PV conservation equations resulting from (2.1) and (2.5) are

$$\frac{\partial q_1}{\partial t}+\frac{\bar V_1}{r}\frac{\partial q_1}{\partial\theta}-\frac{1}{r}\frac{\partial\psi_1}{\partial\theta}\frac{d\bar Q_1}{dr}=0,\qquad \frac{\partial q_2}{\partial t}+\frac{\bar V_2}{r}\frac{\partial q_2}{\partial\theta}-\frac{1}{r}\frac{\partial\psi_2}{\partial\theta}\frac{d\bar Q_2}{dr}=0. \tag{3.2}$$

The perturbations are thought of as associated with an azimuthal integer mode number m and (generally complex) frequency ω,

$$\{q_i(r,\theta,t),\psi_i(r,\theta,t)\}=\{\mathcal{Q}_i(r),\varPhi_i(r)\}e^{i(m\theta-\omega t)}, \tag{3.3}$$

where we suppress the explicit notation of m in $\mathcal{Q}_i(r)$ and $\varPhi_i(r)$ to keep the notation easier; this notation is dropped also in subsequent expressions. Using (3.3) in (3.2) yields the Rayleigh equations,

$$\left(\frac{\bar V_i(r)}{r}-\frac{\omega}{m}\right)\mathcal{Q}_i-\frac{\varPhi_i}{r}\frac{d\bar Q_i}{dr}=0. \tag{3.4}$$

By (2.4) and (3.3), the functions $\mathcal{Q}_i(r)$ and $\varPhi_i(r)$ are related via the equations

$$\mathcal{Q}_1=\frac{d^2\varPhi_1}{dr^2}+\frac{1}{r}\frac{d\varPhi_1}{dr}-\frac{m^2}{r^2}\varPhi_1-\frac{\varLambda^2}{\lambda_1}(\varPhi_1-\varPhi_2), \tag{3.5}$$

$$\mathcal{Q}_2=\frac{d^2\varPhi_2}{dr^2}+\frac{1}{r}\frac{d\varPhi_2}{dr}-\frac{m^2}{r^2}\varPhi_2+\frac{\varLambda^2}{\lambda_2}(\varPhi_1-\varPhi_2). \tag{3.6}$$

Given $\mathcal{Q}_1$ and $\mathcal{Q}_2$, the equations (3.5) and (3.6) for the streamfunctions can be decoupled. The decoupling is possible here, in contrast to its impossibility in equations (2.4), since now the term βr is absent; this is because equations (3.5) and (3.6) deal with the perturbations of the PVs. Consider the barotropic (BT) and baroclinic (BC) streamfunction perturbations,

$$\varPhi_{BT}=\lambda_1\varPhi_1+\lambda_2\varPhi_2,\qquad \varPhi_{BC}=\varPhi_1-\varPhi_2. \tag{3.7}$$

and the corresponding PV perturbations,

$$\mathcal{Q}_{BT}=\lambda_1\mathcal{Q}_1+\lambda_2\mathcal{Q}_2,\qquad \mathcal{Q}_{BC}=\mathcal{Q}_1-\mathcal{Q}_2. \tag{3.8}$$

From equations (3.5) and (3.6) and the definitions (3.7) and (3.8), we get the equations

$$\frac{d^2\varPhi_{BT}}{dr^2}+\frac{1}{r}\frac{d\varPhi_{BT}}{dr}-\frac{m^2}{r^2}\varPhi_{BT}=\mathcal{Q}_{BT} \tag{3.9}$$

$$\frac{d^2\varPhi_{BC}}{dr^2}+\frac{1}{r}\frac{d\varPhi_{BC}}{dr}-\frac{m^2}{r^2}\varPhi_{BC}-\frac{\varLambda^2}{\lambda_1\lambda_2}\varPhi_{BC}=\mathcal{Q}_{BC}, \tag{3.10}$$

where the relation $\lambda_1+\lambda_2=1$ was used in the last equation.

The general solutions to (3.9) and (3.10) can be written as

$$\varPhi_{BT}(r)=\int_R^\infty G_{BT}(r,r')\mathcal{Q}_{BT}(r')dr',\quad \varPhi_{BC}(r)=\int_R^\infty G_{BC}(r,r')\mathcal{Q}_{BC}(r')dr', \tag{3.11}$$

where $G_{BT}(r,r')$ and $G_{BC}(r,r')$ are the barotropic and baroclinic Green functions, respectively. The derivations and expressions for these Green functions appear in Appendix B. From (3.7) we get the expression of the streamfunction in each layer in terms of the barotropic and baroclinic modes,

$$\varPhi_1=\varPhi_{BT}+\lambda_2\varPhi_{BC},\quad \varPhi_2=\varPhi_{BT}-\lambda_1\varPhi_{BC}. \tag{3.12}$$

Using (3.8), (3.11) and (3.12) we get

$$\Phi_1(r) = \int_R^\infty [G_{11}(r,r')\mathcal{Q}_1(r') + G_{12}(r,r')\mathcal{Q}_2(r')]dr' \tag{3.13}$$

$$\Phi_2(r) = \int_R^\infty [G_{21}(r,r')\mathcal{Q}_1(r') + G_{22}(r,r')\mathcal{Q}_2(r')]dr' \tag{3.14}$$

where the four Green functions G_{ij} $(i,j=1,2)$ are defined as

$$G_{11}(r,r') = \lambda_1 G_{BT}(r,r') + \lambda_2 G_{BC}(r,r'), \tag{3.15}$$

$$G_{12}(r,r') = \lambda_2[G_{BT}(r,r') - G_{BC}(r,r')], \tag{3.16}$$

$$G_{21}(r,r') = \lambda_1[G_{BT}(r,r') - G_{BC}(r,r')], \tag{3.17}$$

$$G_{22}(r,r') = \lambda_2 G_{BT}(r,r') + \lambda_1 G_{BC}(r,r'). \tag{3.18}$$

By (3.13) and (3.14), the function G_{ij} is the Green function that connects a PV perturbation at the j-th layer to the streamfunction at the i-th layer. Note also that the boundary condition of no-slip at the cylindrical wall (i.e. $\Phi_1(R) = \Phi_2(R) = 0$ by equations (2.1) and (3.3)) is satisfied by equations (3.13) and (3.14) automatically. Now we express the streamfunctions in terms of the PV perturbations substituting (3.13) and (3.14) into (3.4) and get

$$\frac{m\bar{V}_i(r)}{r}\mathcal{Q}_i - \frac{m}{r}\frac{d\bar{Q}_i(r)}{dr}\int_R^\infty [G_{i1}(r,r')\mathcal{Q}_1 + G_{i2}(r,r')\mathcal{Q}_2]\,dr' = \omega\mathcal{Q}_i(r). \tag{3.19}$$

(3.19) constitute a system of two linear integral equations for the PV perturbations at both layers. In the next section we apply these equations for flows composed of two-layer constant-PV rings.

4. Flows composed of two-layer rings

4.1. *Basic flow profile*

As stated above, for a basic state in the subsequent stability analysis, we take a circularly symmetric flow composed of a uniform-PV ring in each layer. The ring in the upper layer is bounded by the rigid contour at $r = R$ and the material contour at $r = R_1$, which we denote by C_1. Similarly, the ring in the lower layer is bounded by the rigid contour at $r = R$ and the material contour at $r = R_2$, which we denote by C_2. Outside the rings, the PV of each layer equals the background PV. Denoting the PV of the basic flow by $\bar{Q}_i$, and the PV in the upper and lower rings by Γ_1 and Γ_2, respectively, we write

$$\bar{Q}_1(r) = \begin{cases} \Gamma_1, & R \leqslant r \leqslant R_1 \\ 0, & R_1 < r \end{cases}, \quad \bar{Q}_2(r) = \begin{cases} \Gamma_2, & R \leqslant r \leqslant R_2 \\ \beta r, & R_2 < r. \end{cases} \tag{4.1}$$

The PV-jumps across each contour are

$$\Delta_1 = -\Gamma_1, \quad \Delta_2 = \beta R_2 - \Gamma_2. \tag{4.2}$$

The expressions for the basic streamfunctions $\bar{\Psi}_i$ and velocities $\bar{V}_i$ resulting from this PVs configuration are derived in Appendix A. Since the flow is attached to a rigid cylindrical wall (the island), a natural (though not necessary) boundary condition would be the no-slip condition, i.e. the vanishing of the velocity at $r = R$. This condition results from the role of turbulent viscosity in the vicinity of the vertical wall during the formation of the closed flow, as explained in detail in the paper by Rabinovich *et al.* (2018). The vanishing of the velocity at the rigid boundary at $r = R$ imposes a relation between $\mathit{\Gamma}_1$ and $\mathit{\Gamma}_2$ (see Appendix A for details),

$$\mathit{\Gamma}_2 = \frac{-2R^3\beta\lambda_2 + 2R_2^3\beta\lambda_2 + 3\mathit{\Gamma}_1 R^2\lambda_1 - 3\mathit{\Gamma}_1 R_1^2\lambda_1}{3\lambda_2(R_2^2 - R^2)}. \tag{4.3}$$

Schematic profiles of the velocities and PVs at both layers are shown in figure 1.

For future reference we note that equations (4.1) may be written equivalently as

$$\bar{Q}_1(r) = \mathit{\Gamma}_1 + \mathit{\Delta}_1\mathcal{H}(r - R_1), \quad \bar{Q}_2(r) = \mathit{\Gamma}_2 + (\beta r - \mathit{\Gamma}_2)\mathcal{H}(r - R_2), \tag{4.4}$$

where $\mathcal{H}(\cdot)$ is the Heaviside function, which is defined to vanish at zero, $\mathcal{H}(0) = 0$. The gradient of the basic PV profile (4.4) is

$$\frac{d\bar{Q}_1}{dr} = \mathit{\Delta}_1\delta(r - R_1), \quad \frac{d\bar{Q}_2}{dr} = \mathit{\Delta}_2\delta(r - R_2) + \beta\mathcal{H}(r - R_2). \tag{4.5}$$

4.2. *The integral eigenvalue equations*

Define $s_i(r,\theta,t)$ to be the displacement of a particle from its initial reference location at $t = 0$ at the ith layer. Since the PV is conserved as it moves, the change in the PV at the new particle location for small s_i is

$$q_i(r + s_i, \theta, t) = \bar{Q}_i(r,\theta) - \bar{Q}_i(r + s_i, \theta) = -\frac{d\bar{Q}_i}{dr}s_i \tag{4.6}$$

(cf. Bretherton 1966). If all the displacements are associated with an azimuthal integer mode number m and frequency ω as in (3.3), then we may write $s_i = d_i(r)e^{i(m\theta - \omega t)}$ where $d_i(r)$ is the amplitude of the radial displacement of the particle. Comparing (4.6) with (3.3), it is clear that

$$\mathcal{Q}_i(r) = -\frac{d\bar{Q}_i}{dr}d_i(r). \tag{4.7}$$

By (4.5) and (4.7), $\mathcal{Q}_1$ vanishes everywhere except at $r = R_1$, where it is given by a delta function. The displacement s_1 of a particle at $r = R_1$ can also be interpreted as the deformation of C_1 (cf. Kizner *et al.* 2013; Rabinovich *et al.* 2018); the amplitude $d_1(R_1)$ of C_1's perturbation is denoted by α_1/R_1. Similarly, the amplitude $d_2(R_2)$ of C_2's perturbation at $r = R_2$ is denoted by α_2/R_2. The amplitude of the displacement $d_2(r)$ at the outer region $r > R_2$ in the lower layer is denoted by $\eta(r)/r$, and can be viewed as deformation of the background constant-PV contours (which are circles). The division by R_1, R_2 and r is made in order to make the integral operator symmetric, which is useful as is shown below (§6). Therefore, using (4.5) and (4.7), we write

$$\mathcal{Q}_1 = -\frac{\mathit{\Delta}_1\alpha_1}{R_1}\delta(r - R_1), \quad \mathcal{Q}_2 = -\frac{\mathit{\Delta}_2\alpha_2}{R_2}\delta(r - R_2) - \frac{\beta}{r}\eta(r)\mathcal{H}(r - R_2). \tag{4.8}$$

Inserting (4.8) into the eigenvalue integral equations (3.19) yields the following three eigenvalue equations,

$$\frac{\bar{V}_1(R_1) - \mathit{\Delta}_1 G_{11}(R_1,R_1)}{R_1}\alpha_1 - \frac{\mathit{\Delta}_1 G_{12}(R_1,R_2)}{R_2}\alpha_2 - \beta\mathit{\Delta}_1\int_{R_2}^{\infty}\frac{G_{12}(R_1,r')}{r'}\eta(r')dr' = \frac{\omega}{m}\alpha_1, \tag{4.9}$$

$$-\frac{\mathit{\Delta}_2 G_{21}(R_2,R_1)}{R_1}\alpha_1 + \frac{\bar{V}_2(R_2) - \mathit{\Delta}_2 G_{22}(R_2,R_2)}{R_2}\alpha_2 - \beta\mathit{\Delta}_2\int_{R_2}^{\infty}\frac{G_{22}(R_2,r')}{r'}\eta(r')dr' = \frac{\omega}{m}\alpha_2, \tag{4.10}$$

$$-\frac{G_{21}(r,R_1)}{R_1}\alpha_1-\frac{G_{22}(r,R_2)}{R_2}\alpha_2+\frac{\bar{V}_2(r)}{r}\eta(r)-\beta\int_{R_2}^{\infty}\frac{G_{22}(r,r')}{r'}\eta(r')dr'=\frac{\omega}{m}\eta(r). \quad (4.11)$$

Equations (4.9)-(4.11) can be recast to a standard matrix eigenvalue equation; it is then solved numerically using the 'eig' function in Matlab, which uses the QZ algorithm (Moler & Stewart 1973). To get the matrix form, the integrals are approximated via a Gaussian quadrature rule (e.g Hildebrand 1987), which for any function $f(x)$ takes the form $\int_{R_2}^{\infty} f(r)dr \approx \sum_{i=1}^{N} w_i f(r_i)$; here r_i and w_i are the nodes and weights, respectively, of the quadrature rule employed.

Since the domain is infinite, we divided the integral into two regions: The first one is the close neighborhood of the island, where the basic flow velocities at the two layers are significant. Outside the largest ring the velocities drop exponentially with r with typical length scale $\Lambda/\sqrt{\lambda_1\lambda_2}$ (see Appendix A); thus the velocities remain significant at $R_2 \leqslant r \leqslant \max(R_1,R_2)+5\Lambda/\sqrt{\lambda_1\lambda_2}$. In this region, the Legendre-Gauss Quadrature rule is applied with 1000 points. The second region is outside, at $\max(R_1,R_2)+5\Lambda/\sqrt{\lambda_1\lambda_2} < r < \infty$, where the Gauss-Laguerre quadrature rule is applied with 150 points. Tests of convergence show that the results are robust; e.g., even with half the number of points in each region, the error in calculating the eigenvalues, is less than 0.1%.

5. The resonance viewpoint

The integral eigenvalue equations (4.9)-(4.11) allow direct interpretation of the couplings that occur in the system studied. We demonstrate it using the first equation, (4.9), which determines the angular velocity of the upper contour C_1 perturbation, at $r = R_1$. The RHS of (4.9) may be viewed also as the time derivative of the PV perturbation at $r = R_1$ since the time derivative is proportional to ω (cf. equation (3.3)). The first term in the LHS of (4.9) contains the free-streaming term $\bar{V}_1(R_1)\alpha_1/R_1$ with the coupling to the basic PV jump at its place, $-\Delta_1 G_{11}(R_1,R_1)\alpha_1/R_1$. This term would determine the angular velocity of the PV contour at $r = R_1$ if no other couplings occur (cf. Kamp 1991). The next term represents the coupling between the PV perturbations at C_1 and C_2, since it is α_2 that influences the time development of α_1. Finally, the integral term represents the influence of the PV perturbation $\eta(r)/r$ in the lower layer outside C_2 on the evolution of C_1's perturbation.

The identification of each of the coupling terms can now by applied in case that instability is reached. By allowing only certain couplings to remain in the equations while removing others, one can isolate different subsystems of the entire system and find the dominant ones. These are the couplings that lead to the closest phase velocity and growth rate of the fully coupled system. In this case the PV perturbations that couple to cause the instability are said to be resonant.

The resonance viewpoint has been employed by many authors for shallow water systems, as mentioned in the Introduction. Usually it is demonstrated by the crossing of two dispersion curves (Cairns 1979); here another method is employed in the QG case, i.e. the method of finding the dominant couplings in the eigenvalue equations written in terms of the PVs. In §7 it is shown that the results are consistent with those of the crossing dispersion curve method.

In the resonant viewpoint the instability is caused by the interaction of two waves which phase-lock and enhance the growth of each other (e.g. Heifetz *et al.* 1999; Rabinovich *et al.* 2018). For the basic flow considered in this paper there are three Rossby waves which can interact: the first one travels along C_1 (where the PV in the upper layer jumps), the second one travels along C_2, and the third one, which exists due to the bottom topography, travels at the outer region in the second layer $r > R_2$. As is discussed in

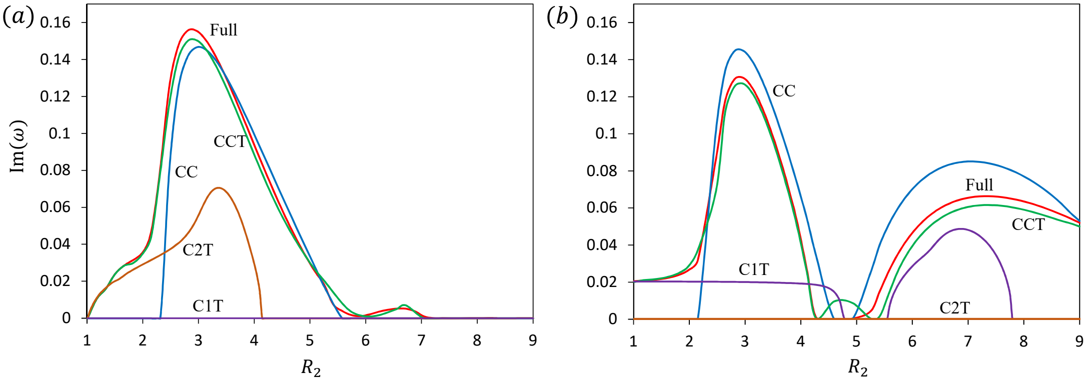

Figure 2: Growth rates $\mathrm{Im}(\omega)$ for different couplings as functions of R_2 at $R_1 = 5, \beta = -0.1, m = 2, \mathit{\Lambda} = 1$, and $\lambda_1 = \lambda_2 = 0.5$ for (a) $\mathit{\Gamma}_1 = 1$, (b) $\mathit{\Gamma}_1 = -1$. The types of couplings are: Full (red), CC (blue), C1T (purple), C2T (brown), CCT (green).

§6, there are various perturbation types for this third wave, which we collectively call 'topographic' perturbations. Using the eigenvalue equations (4.9)-(4.11) we identify four types of instability:

(i) Contour-contour (CC) instability: in this case the dominant interaction which leads to instability is the interaction between the perturbations at the rings' periphery, i.e. between C_1 and C_2. The coupling the contours C_1 and C_2 alone corresponds to setting $\beta = 0$ in (4.9)-(4.11), thus remaining with two algebraic equations to be solved. In §7 this instability is presented in more detail.

(ii) Contour C_1-topography ($\mathrm{C_1T}$) instability: in this case the CC subsystem (composed of C_1 and C_2 alone) is stable, i.e. the PV jumps alone are not the cause to instability, but rather the resonance of the wave at C_1 with the topographic PV perturbations in the lower layer (in the region $r > R_2$). The eigenvalue calculation in this case is achieved by setting $\alpha_2 = 0$ in equations (4.9)-(4.11).

(iii) Contour C_2-topography ($\mathrm{C_2T}$) instability: in this case the wave at the lower layer PV contour resonates with the PV topographic perturbations outside. The eigenvalue calculation in this case is achieved by setting $\alpha_1 = 0$ in equations (4.9)-(4.11).

(iv) Both contours-topography (CCT) instability: in this case the dominant resonance is between one of the neutral perturbation types of the mutual contours subsystem CC and the topographic perturbations. The eigenvalue calculation in this case is achieved by rearranging the equations (4.9)-(4.11) in such a way that the perturbations of the CC subsystem are decoupled; this is explained in §7.2. We note that although it seems that the entire system takes part in this instability, this is not so: only one of the neutral CC perturbation types participates in this resonance, while the other one is not.

In the following, we collectively term (ii)-(iv) as contours-topography (CT) instabilities; these are discussed in §7 in more detail. Figure 2 presents an example showing the identification of the instability types; the growth rates (i.e. $\mathrm{Im}(\omega)$) are shown for each of the above resonances, as a function of the radius of the lower-layer ring. The flow parameters are $\beta = -0.1, R_1 = 5, \lambda_1 = \lambda_2 = 1/2$, and $\mathit{\Gamma}_1 = 1$ (figure 2a) or $\mathit{\Gamma}_1 = -1$ (figure 2b).

In the case of $\mathit{\Gamma}_1 = 1$ (figure 2a), the CC resonance is dominant when $2.3 < R_2 < 5.5$, while the C_2T resonance is dominant when $R_2 < 2$. The C_1T resonance is totally absent in this case; the explanation is given below (§5.1). The growth rates of the CC instability are generally higher than those of the C_2T instability. Also, there is a small 'window' at $2 < r < 2.3$ where the CC interaction is stable while the C_2T interaction is not; yet, the growth rate of the full instability is much higher (up to 4 times) than the growth rate of the C_2T resonance and therefore cannot be attributed to this resonance. The dominant instability in this region is of type CCT.

In the case of $\mathit{\Gamma} = -1$ (figure 2b), again the CC resonance admits the highest growth rates and is dominant in most values of R_2. In much of the CC instability region, the actual (full-system) growth rate is lower than that implied by growth rate of the CC interaction. Therefore, the topography in this case stabilizes the flow. Again at small values of R_2 (below 1.5) the dominant resonance is between one of the contours and the topographic perturbations, but this time it is of type C_1T and the C_2T type is absent. At small region at $1.5 < r < 2.1$ again the instability is of type CCT.

5.1. *Pseudomomentum considerations*

As is known, while momentum is not a conserved quantity in the system of the linearized equations (3.2), one can define an analogous quantity that is conserved, the pseudomomentum (Vallis 2017). While a necessary condition for instability to occur is phase locking, i.e. crossing of the dispersion curves of two neutral waves, not every crossing leads to instability. As shown by Sakai (1989), an additional requirement for instability is that the two waves would have opposite signs of pseudomomentum.

The expression for the pseudomomentum density in the two layer model on the beta cone (i.e. in polar coordinates where the basic flow is radially symmetric) is developed in Appendix C and is given by the following expression,

$$\mathcal{M} = -\frac{\lambda_1}{2}\frac{d\bar{Q}_1}{dr}\langle s_1^2\rangle - \frac{\lambda_2}{2}\frac{d\bar{Q}_2}{dr}\langle s_2^2\rangle, \tag{5.1}$$

where the brackets $\langle\cdot\rangle$ denote that the azimuthally averaged value of the variable is taken. The pseudomomentum density satisfies the continuity equation

$$\frac{\partial\mathcal{M}}{\partial t} + \frac{1}{r}\frac{\partial\mathcal{F}}{\partial r} = 0, \tag{5.2}$$

where $\mathcal{F} = \langle\frac{\partial\psi_1}{\partial\theta}\frac{\partial\psi_1}{\partial r}\rangle$ is the Eliaseen-Palm (EP) flux. If equation (5.2) is integrated over the entire plane outside the island ($r > R$), we get the equation for pseudomomentum conservation, $\frac{\partial M}{\partial t} = 0$, where

$$M = \int_R^\infty r\mathcal{M}dr = -\int_R^\infty \left(\frac{\lambda_1}{2}\frac{d\bar{Q}_1}{dr}\langle s_1^2\rangle + \frac{\lambda_2}{2}\frac{d\bar{Q}_2}{dr}\langle s_2^2\rangle\right)dr \tag{5.3}$$

Since M is conserved, in case of an instability it must vanish. This leads to the known Rayleigh's necessary condition for instability, that the basic PV gradient must be somewhere negative and somewhere positive (cf. Pedlosky 1964; Solodoch *et al.* 2016). Moreover, in case that only two perturbation types resonate, their pseudomomenta must have opposite signs (Sakai 1989).

For the basic flow considered in this paper, using (4.5) and (4.8), the pseudomomentum becomes

$$M = \left(-\frac{\lambda_1\mathit{\Delta}_1}{4R_1^2}|\alpha_1|^2 - \frac{\lambda_2\mathit{\Delta}_2}{4R_2^2}|\alpha_2|^2 - \int_R^\infty \frac{\lambda_2\beta}{4r^2}|\eta|^2dr\right)e^{2\mathrm{Im}(\omega)t}. \tag{5.4}$$

Since the PV jumps at the two contours C_1 and C_2 are opposite in sign, their pseudomomenta are opposite in sign and the Rossby waves traveling along these contours may resonate. The pseudomomentum of the perturbation at the exterior region $r > R_2$ is always positive, β being always negative. Therefore the exterior perturbations can only resonate with the contour wave whose pseudomomentum is negative, i.e. is traveling along a positive PV gradient.

This explains why only one contour wave resonates with the topographic perturbations as shown in figure 2. If $\mathit{\Gamma}_1 = 1$, the pseudomomentum of the contour wave at $r = R_1$ is positive (since $\mathit{\Delta}_1 < 0$ by (4.2))), while that of the contour wave at $r = R_2$ is negative (since $\mathit{\Delta}_2 > 0$ for the specific parameters chosen by (4.2)). Thus only the lower-layer contour has opposite sign of pseudomomentum relative to that of the outside perturbations (which is always positive); therefore $\mathrm{C_1T}$ instability is impossible in this case (figure 2a). The same argument explains why $\mathrm{C_2T}$ instability is impossible in the case $\mathit{\Gamma}_1 = -1$ (figure 2b).

6. The perturbation types in the outer region

We now focus on the subsystem of the basic flow outside the liquid contours, i.e. we search for modes whose perturbation is dominant (i.e., strong relative to the contours' perturbations) at the lower layer at $r > R_2$. For this, we assume that the PV jumps at any of the liquid contours is negligible ($\mathit{\Delta}_1 \approx \mathit{\Delta}_2 \approx 0$), thus avoiding any coupling to waves at that contours. The resulting PV perturbations can be seen as self-excitations of the outer region , caused by the presence of the topography. Physically, as a consequence, the contours may oscillate and resonate to yield the contours-topography instability which is discussed in §7.

Neglecting α_1 and α_2 in (4.9)-(4.11) yields a single integral equations for η,

$$\frac{\bar{V}_2(r)}{r}\eta(r) - \beta \int_{R_2}^{\infty} \frac{G_{22}(r,r')}{r'}\eta(r')dr' = \frac{\omega}{m}\eta(r). \tag{6.1}$$

Since the kernel $\frac{G_{22}(r,r')}{r'}$ is symmetric (see Appendix B), the operator on the left hand side of the equation, acting on $\eta(r)$, is symmetric; therefore the eigenvalues are necessarily real. The eigenfunctions are orthogonal with respect to the standard inner product defined by $\langle f_1, f_2\rangle = \int_{R_2}^{\infty} f_1(r) f_2^*(r)dr$ for any two functions f_1 and f_2, for which this integral is convergent. This integral equation (6.1) is similar in form to the integral equation of a barotropic flow discussed in detail by Kamp (1991). Here the Green function is different due to the cylindrical symmetry and, more importantly, due to the baroclinic component of the Green function (see (3.18)). Another difference is the fact that the domain here is unbounded.

Equation (6.1) was solved numerically using the numerical scheme described at the end of §4.2. The frequency ω was indeed found to be always real, and some eigenfunctions examples found are shown in figure 3. The properties of the spectrum and the eigenfunctions are explained analytically below.

Before dwelling into the solutions structure, a rough estimate of the allowed frequencies (the spectrum) may be carried out. Multiplication of equation (6.1) by η^* and integrating yields

$$\int_{R_2}^{\infty} \frac{\bar{V}_2(r)}{r}|\eta(r)|^2 dr - \beta \int_{R_2}^{\infty}\int_{R_2}^{\infty} \frac{G_{22}(r,r')}{r'}\eta^*(r')\eta(r)dr'dr = \frac{\omega}{m}\int_{R_2}^{\infty} |\eta(r)|^2 dr. \tag{6.2}$$

Since the term $\frac{G_{22}(r,r')}{r'}$ is always negative (by (3.18), (B 6) and (B 12)), the second

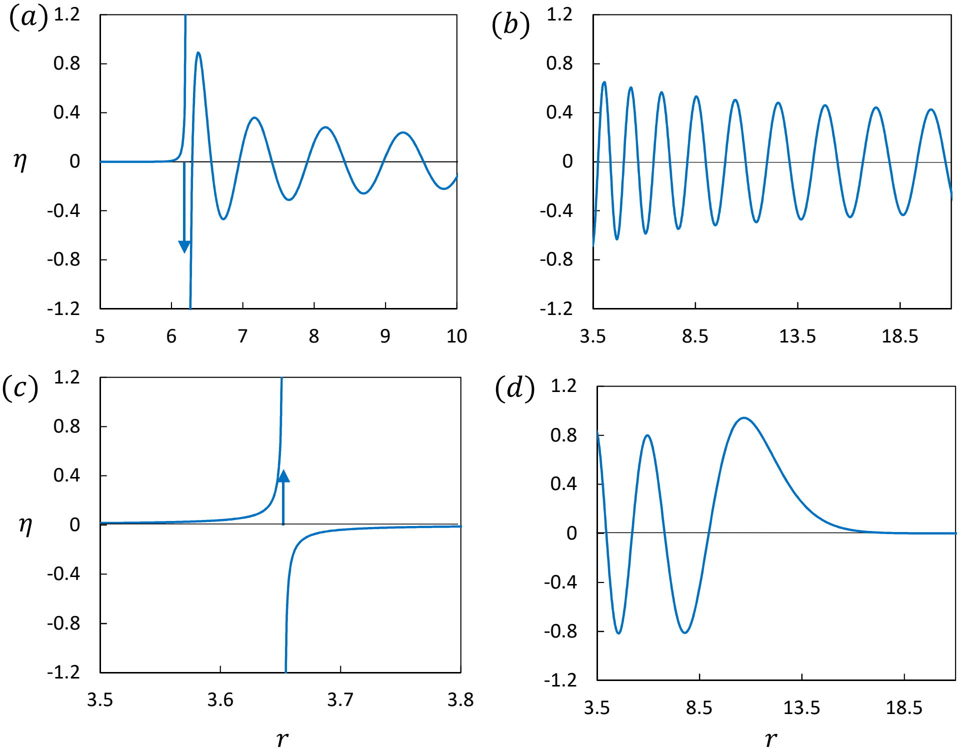

Figure 3: Examples of perturbation types at the outer region $r > R_2$. The shared flow parameters are $\beta = -0.1, \Lambda = 1, \lambda_1 = \lambda_2 = 0.5, m = 3$. Arrow designates a delta function. (a) asymptotically wavelike barotropic mode with critical layer ($R_1 = 4, R_2 = 5, \Gamma_1 = 1$), (b) asymptotically wavelike barotropic mode without critical layer ($R_1 = 2, R_2 = 3.5, \Gamma_1 = -1$), (c) asymptotically evanescent barotropic mode with critical layer ($R_1 = 2, R_2 = 3.5, \Gamma_1 = -1$), (d) asymptotically baroclinic mode without critical layer ($R_1 = 2, R_2 = 3.5, \Gamma_1 = -1$). Arrows denote delta functions, their height corresponds to the multiplicative factor in front of the delta functions.

integral in the LHS is negative; therefore the possible values of ω are

$$-\infty < \omega < \sup_r \frac{m\bar{V}_2(r)}{r}, \tag{6.3}$$

where 'sup' denotes the supremum. For future reference we define the segments

$$\mathcal{S}_1 = \left(\inf_r \frac{m\bar{V}_2(r)}{r}, \sup_r \frac{m\bar{V}_2(r)}{r}\right), \quad \mathcal{S}_2 = \left(-\infty, \inf_r \frac{m\bar{V}_2(r)}{r}\right), \tag{6.4}$$

so by (6.3), $\omega \in \mathcal{S}_1 \cup \mathcal{S}_2$. We note that contrary to the derived bounds on the phase velocity given by Solodoch *et al.* (2016) for annular flows (known as the semi-circle theorems, cf. Pedlosky (1964)), the phase velocity here cannot, by similar arguments, be bounded from below. The reason is that the flow is unbounded, whereas such theorems use the fact that it is confined to a channel (zonal or annular).

6.1. *Structure of the solution near a critical layer*

In a case that $\omega \in \mathcal{S}_1$ there is a critical distance r_c at which the angular velocity of the perturbation, ω/m, is equal to the angular velocity of the flow, $V(r_c)/r_c$; the integral equation (6.1) is then singular. In this case the solution contains a critical layer (see e.g. Adam 1986). The left hand side of the equation can be viewed as a sum of an operator of multiplication by $\bar{V}_2/r$ and an integral operator. Following Van Kampen (1955) and Kamp (1991), the solution is written in the form of a delta function (the eigenfunction of the multiplication operator) plus an additional term,

$$\eta(r) = D(\omega)\delta\left(\frac{\bar{V}_2}{r} - \frac{\omega}{m}\right) - P\frac{\beta}{\frac{\bar{V}_2}{r} - \frac{\omega}{m}}\xi(r), \tag{6.5}$$

where $D(\omega)$ and $\xi(r)$ are unknown functions to be specified, and $\xi(r)$ is assumed to be a regular function of r; P signifies that the principal value of the integral is to be taken when integrating the last expression with respect to r, i.e. $P\int_R^\infty = \lim_{\epsilon\to 0}(\int_R^{r_c-\epsilon} + \int_{r_c+\epsilon}^\infty)$. Some of the solutions we found numerically are indeed of the form (6.5), as can be shown in figures 3a and 3c; the PV perturbation blows up near the point $r = r_c$ and a delta function appears at $r = r_c$. We note that equation (6.5) is valid also if there is no r for which $V(r)/r = \omega/m$, since then there is no critical layer and we may set $D(\omega) = 0$; these are regular solutions as shown in figures 3b and 3d.

Plugging (6.5) into (6.1) yields the following equation for ξ,

$$\xi(r) = -\frac{D(\omega)G_{22}(r, r_c)}{|(V(r)/r)'_{r_c}|r_c} + P\int_{R_2}^{\infty}\frac{\beta G_{22}(r, r')}{(\frac{\bar{V}_2(r')}{r'} - \frac{\omega}{m})r'}\xi(r')dr' \tag{6.6}$$

where we assume for simplicity that at $r > R_2$ the function V_2/r is injective and $r_c = (V_2/r)^{-1}(\omega/m)$, as is the case for the basic flows considered in this paper. Also, we used the mathematical relation $\delta(f(x)) = \delta(x - x_0)/|f'(x_0)|$ that holds for any smooth injective function $f(x)$, where x_0 is a root of $f(x)$ (if exist, else $\delta(f(x)) = 0$). Since (6.1) is homogeneous, we can arbitrarily demand that

$$\int_{R_2}^{\infty}\eta(r')dr' = 1, \tag{6.7}$$

which, by (6.5), is equivalent to the specification of the function $D(\omega)$ by the following equation,

$$\frac{D(\omega)}{|(V(r)/r)'_{r_c}|} - P\int_{R_2}^{\infty}\frac{\beta}{\frac{\bar{V}_2(r')}{r'} - \frac{\omega}{m}}\xi(r')dr' = 1. \tag{6.8}$$

Using (6.8) in (6.6), we get that ξ satisfies the following nonsingular inhomogeneous Fredholm equation of the second kind,

$$\xi(r) = -\frac{G_{22}(r, r_c)}{r_c} + \beta\int_{R_2}^{\infty}\frac{G_{22}(r, r')/r' - G_{22}(r, r_c)/r_c}{\frac{\bar{V}_2(r')}{r'} - \frac{\omega}{m}}\xi(r')dr'. \tag{6.9}$$

The non-singularity is guaranteed since the Green functions' derivative is always much lower than the velocity's derivative (inverse power vs. linear function of r, see Appendices A and B). Since there is no singularity in this equation at $r = r_c$, the function $\xi(r)$ is regular as assumed. If ω is outside the range of $\{mV(r)/r\}$ then the solution consists only of the regular function $\xi(r)$ with no blow-up.

Equation (6.9) can be transformed to a fourth-order non-homogeneous (homogeneous) differential equation if a critical layer exists (not exists) by the procedure presented in Appendix D. The non-homogeneous term (D 6) that appears in the resulting differential equation (D 5) contains only a delta function with its derivatives, that are singular only at $r = r_c$ (if exists). Therefore, asymptotically at $r \to \infty$ the solutions to the differential equation have the same form, whether there is a critical layer or not. We denote the four linearly independent regular solutions to the equation by h_1, h_2, h_3 and h_4. In the following section we find asymptotic expressions for h_j $(j = 1..4)$ and find the spectrum properties of the eigenvalue equation (6.1).

6.2. *Asymptotically barotropic and baroclinic wave types*

We now show that there are two types of solutions, that asymptotically, at large r, behave as barotropic and baroclinic waves. For this we resort to the equations in their differential form, equation (3.4), and consider it far from the origin, where $\bar{V}_2$ can be neglected; since the velocity diminishes exponentially with r (see equations (A 20)-(A 21)), it is always possible to find such range. By (3.4), far from the origin, $\mathcal{Q}_1 = 0$ and $\mathcal{Q}_2 = -m\beta\Phi_2/\omega r$, so equations (3.5) and (3.6) become

$$0 = \frac{d^2\Phi_1}{dr^2} + \frac{1}{r}\frac{d\Phi_1}{dr} - \frac{m^2}{r^2}\Phi_1 - \frac{\Lambda^2}{\lambda_1}(\Phi_1 - \Phi_2), \tag{6.10}$$

$$-\frac{m\beta\Phi_2}{\omega r} = \frac{d^2\Phi_2}{dr^2} + \frac{1}{r}\frac{d\Phi_2}{dr} - \frac{m^2}{r^2}\Phi_2 + \frac{\Lambda^2}{\lambda_2}(\Phi_1 - \Phi_2). \tag{6.11}$$

Asymptotically we may neglect the left hand side of (6.11) since Φ_2 appears in the right hand side without division by r. We use the ansatz $\Phi_2 = a\Phi_1$ where a is some parameter to be determined. As is shown below, this ansatz leads to four independent solutions, which by the abovesaid at the end of §6.1, cover all the possible asymptotic solutions of the fourth order differential equation. Plugging $\Phi_2 = a\Phi_1$ in equations (6.10) and (6.12) we get the set of equations (after dividing the second equation by a),

$$0 = \frac{d^2\Phi_1}{dr^2} + \frac{1}{r}\frac{d\Phi_1}{dr} - \frac{m^2}{r^2}\Phi_1 - \frac{\Lambda^2}{\lambda_1}(1-a)\Phi_1, \tag{6.12}$$

$$0 = \frac{d^2\Phi_1}{dr^2} + \frac{1}{r}\frac{d\Phi_1}{dr} - \frac{m^2}{r^2}\Phi_1 + \frac{\Lambda^2}{\lambda_2}\frac{(1-a)}{a}\Phi_1. \tag{6.13}$$

These two equations are identical provided that

$$\frac{1-a}{\lambda_2 a} = -\frac{1-a}{\lambda_1} \quad \Rightarrow \quad a = 1 \ \text{ or } \ a = -\frac{\lambda_1}{\lambda_2}. \tag{6.14}$$

So, asymptotically, $\Phi_2 \sim \Phi_1$ or $\Phi_2 \sim -\frac{\lambda_1}{\lambda_2}\Phi_1$. The first corresponds to the asymptotically barotropic mode, where $\Phi_{BC} = \Phi_1 - \Phi_2 \approx 0$, and the second one to the asymptotically baroclinic mode, where $\Phi_{BT} = \lambda_1\Phi_1 + \lambda_2\Phi_2 \approx 0$. In the following we loosely term perturbations whose asymptotic behavior is barotropic (baroclinic) as barotropic (baroclinic) modes, without repeating the fact that this behavior is only asymptotic. Also, it should be stressed that barotropic or baroclinic character of the mode is reflected only in the streamfunctions and not via the relations between the PV perturbations, since the PV perturbation at the upper layer is zero in any case; thus the barotropic and baroclinic PV perturbations are $\mathcal{Q}_{BT} = \lambda_2\mathcal{Q}_2$ and $\mathcal{Q}_{BC} = -\mathcal{Q}_2$, i.e. they are of the same order of magnitude. Having arrived to the conclusion that there are two kinds of asymptotic modes, we turn now to find their r-dependence.

6.2.1. *Barotropic mode*

First, we assume that the barotropic component of the streamfunction is the dominant one, $\Phi_{BT} \gg \Phi_{BC}$ (i.e., $\Phi_1 \approx \Phi_2$). By (3.11), this means that

$$\int_{R_2}^{\infty} \frac{G_{BT}(r,r')}{r'}\eta(r')dr' \gg \int_{R_2}^{\infty} \frac{G_{BC}(r,r')}{r'}\eta(r')dr', \tag{6.15}$$

so we take only the barotropic component of the Green function in equation (6.1),

$$\frac{\bar{V}_2(r)}{r}\eta(r) - \beta \int_{R_2}^{\infty} \frac{\lambda_2 G_{BT}(r,r')}{r'}\eta(r')dr' = \frac{\omega}{m}\eta(r). \tag{6.16}$$

We impose the linear operator D_1 defined by (D 1) on both sides of (6.16) and use (D 2); the term $\mathrm{D}_1(\frac{\bar{V}_2(r)}{r}\eta(r))$ is neglected, since the basic velocity and its derivatives are negligible far from the island (see Appendix A). The integral equation is then converted to the following differential equation,

$$\frac{\eta(r)}{r} = -\frac{\omega}{m\beta\lambda_2}\left(\frac{d^2\eta}{dr^2} + \frac{1}{r}\frac{d\eta}{dr} - \frac{m^2}{r^2}\eta\right). \tag{6.17}$$

If $\omega < 0$, the general solution to (6.17) is given by

$$\eta(r) = AH_{2m}^{(1)}\left(2\sqrt{\frac{m\beta\lambda_2 r}{\omega}}\right) + BH_{2m}^{(2)}\left(2\sqrt{\frac{m\beta\lambda_2 r}{\omega}}\right), \tag{6.18}$$

where $H_{2m}^{(1)}$ and $H_{2m}^{(1)}$ are the Hankel functions of the first kind and second kind, respectively, of order $2m$. Referring to abovesaid at the end of §6.2, we denote the two regular solutions to (D 5), that $H_{2m}^{(1)}$ and $H_{2m}^{(2)}$ are their asymptotic approximation, by h_1 and h_2, respectively. The solutions must obey the radiation condition, according to which energy cannot arrive from outside; this no-radiation condition is satisfied only by $H_{2m}^{(1)}$, so $B = 0$ (see Rabinovich *et al.* (2019) for details). The solution to (6.16) is then in the form

$$\eta(r) = Ah_1(r;\omega) + D(\omega)\delta(\bar{V}_2/r - \omega/m), \tag{6.19}$$

where asymptotically $h_1(r;\omega) \sim H_{2m}^{(1)}\left(2\sqrt{m\beta\lambda_2 r/\omega}\right)$ and $D(\omega)$ is nonzero if there is a critical layer, and zero otherwise. Substitution of (6.19) in (6.16) and applying the equation at $r = R_2$ leads to two options: if $\omega \in \mathcal{S}_1$, i.e. $D(\omega) \neq 0$, then A is nonzero and is determined by an inhomogeneous equation. Therefore, for any $\omega \in \mathcal{S}_1$ there is a solution. Such a solution, having a critical layer and asymptotically barotropic, is shown in figure 3a. On the other hand, if there is no critical layer then $D(\omega) = 0$, and the equation is homogeneous in A. Therefore, in this case ω can take only discrete values in the segment $\mathcal{S}_2$. Such an asymptotically barotropic solution without a critical layer is shown in figure 3b.

If $\omega > 0$, the general solution to (6.17) is given by a superposition of the modified Bessel functions of order $2m$,

$$\eta(r) = \tilde{A}K_{2m}\left(2\sqrt{-\frac{m\beta\lambda_2 r}{\omega}}\right) + \tilde{B}I_{2m}\left(2\sqrt{-\frac{m\beta\lambda_2 r}{\omega}}\right). \tag{6.20}$$

These two functions are the asymptotic approximations to h_1 and h_2 in this case. For the solutions to be limited as $r \to \infty$, we must set $\tilde{B} = 0$. In virtue of (6.3), the case $\omega > 0$ occurs only if $\bar{V}_2$ is positive, in which case it is approaching 0 at infinity (see Appendix

A). Therefore $\omega \in \mathcal{S}_1$ and this type of perturbation always contains a critical layer,

$$\eta(r) = Ah_1(r;\omega) + D(\omega)\delta(\bar{V}_2/r - \omega/m), \tag{6.21}$$

with $D(\omega) \neq 0$. An example of this solution is shown in figure 3c. Substitution of (6.21) in (6.16) and applying the equation at $r = R_2$ leads to a determination of $A \neq 0$ with no limitation on ω. Therefore, ω can take any value in the segment $\mathcal{S}_1$.

6.2.2. *Baroclinic mode*

Now we turn to the case where the baroclinic component is dominant. In this case, by (6.1),

$$\int_{R_2}^{\infty} \frac{\lambda_1 G_{BC}(r,r')}{r'}\eta(r')dr' = -\frac{\omega}{m\beta}\eta(r). \tag{6.22}$$

We impose the linear operator D_2 defined by (D 1) on both sides of (6.22) and get, using (D 2),

$$\frac{\eta(r)}{r} = -\frac{\omega}{m\beta\lambda_1}\left(\frac{d^2\eta}{dr^2} + \frac{1}{r}\frac{d\eta}{dr} - \frac{m^2}{r^2}\eta - \frac{\varLambda^2}{\lambda_1\lambda_2}\eta\right). \tag{6.23}$$

The general solution to (6.23) is

$$\eta(r) = \frac{E}{\sqrt{r}}W_{\kappa,m}\left(\frac{2\varLambda r}{\sqrt{\lambda_1\lambda_2}}\right) + \frac{F}{\sqrt{r}}M_{\kappa,m}\left(\frac{2\varLambda r}{\sqrt{\lambda_1\lambda_2}}\right), \tag{6.24}$$

where $\kappa = \frac{m\beta\lambda_1\sqrt{\lambda_1\lambda_2}}{2\varLambda\omega}$, and $W_{\kappa,m}$ and $M_{\kappa,m}$ are the Whittaker functions of order (κ, m); E and F are constants. Using the Whittaker functions' asymptotic form (Whittaker & Watson 1996), asymptotically we get

$$\eta(r) \sim Er^{\kappa-\frac{1}{2}}e^{-\frac{\varLambda r}{\lambda_1\lambda_2}} + Fr^{-\kappa-\frac{1}{2}}\frac{\varGamma(1+2m)}{\varGamma(\frac{1}{2}+m-\kappa)}e^{\frac{\varLambda r}{\lambda_1\lambda_2}}. \tag{6.25}$$

For the solution to be limited as $r \to \infty$, we set $F = 0$. It is known that $W_{k,m}$ has positive zeros only if $\kappa > 1/2$ (Wimp 1965). This inequality yields $m\beta\sqrt{\lambda_1\lambda_2}/\varLambda \leqslant \omega < 0$, i.e. only negative eigenvalues yield a wavelike asymptotic eigenfunctions, an example of which is shown in figure 3d.

Referring to abovesaid at the end of §6.2, we denote the two regular solutions to (D 5), that $W_{\kappa,m}\left(2\varLambda r/\sqrt{\lambda_1\lambda_2}\right)/\sqrt{r}$ and $M_{\kappa,m}\left(2\varLambda r/\sqrt{\lambda_1\lambda_2}\right)/\sqrt{r}$ are their asymptotic approximation, by h_3 and h_4, respectively. The general solution to (6.22) is then in the form

$$\eta(r) = Eh_3(r;\omega) + D(\omega)\delta(\bar{V}_2/r - \omega/m), \tag{6.26}$$

where asymptotically $h_3(r;\omega) \sim H_{2m}^{(1)}\left(2\sqrt{m\beta\lambda_2 r/\omega}\right)$ and where $D(\omega)$ is nonzero if there is a critical layer and zero otherwise. Substitution of (6.26) in (6.22) and applying the equation at $r = R_2$ leads, as in the barotropic case, to to two options: if $\omega \in \mathcal{S}_1$, i.e. $D(\omega) \neq 0$, then E is nonzero and is determined by an inhomogeneous equation. Therefore, for any $\omega \in \mathcal{S}_1$ there is a solution. On the other hand, if there is no critical layer then $D(\omega) = 0$, and the equation is homogeneous in E. Therefore, in this case ω can take only discrete values in the segment $\mathcal{S}_2$. Such an asymptotically baroclinic solution without critical layer is shown in figure 3d. The solution is wavelike in some region and then, starting from some distance, decays exponentially in r as implied by (6.25).

A summary of the different parts of the spectrum is listed in table 1. One part consists of all the values in the segment $\mathcal{S}_1$ (excluding zero), where each value has multiplicity 2, i.e. there are two corresponding eigenfunctions with a critical layer. These eigenfunctions

segment containing ω	ω sign	asymptotic mode	asymptotic form	spectrum is continuous/ discrete
$\mathcal{S}_1$	$\omega > 0$	BT	$CK_{2m}(2\sqrt{m\beta\lambda_2 r/\omega})$	continuous
$\mathcal{S}_1$	$\omega < 0$	BT	$AH^{(1)}_{2m}(2\sqrt{m\beta\lambda_2 r/\omega})$	continuous
$\mathcal{S}_1$	any $\omega \neq 0$	BC	$EW_{\kappa,m}(2\Lambda r/\sqrt{\lambda_1\lambda_2})/\sqrt{r}$	continuous
$\mathcal{S}_2$	$\omega < 0$	BT	$AH^{(1)}_{2m}(2\sqrt{m\beta\lambda_2 r/\omega})$	discrete
$\mathcal{S}_2$	any $\omega \neq 0$	BC	$EW_{\kappa,m}(2\Lambda r/\sqrt{\lambda_1\lambda_2})/\sqrt{r}$	discrete

Table 1: Parts of the spectrum and their properties. The segments $\mathcal{S}_1$ and $\mathcal{S}_2$ are defined by (6.4). *BT* and *BC* designate barotropic mode and baroclinic mode, respectively.

correspond asymptotically to barotropic or baroclinic forms. These are evanescent if $\omega > 0$. In case that $\omega < 0$, the asymptotically barotropic type is wavelike as $r \to \infty$ and the asymptotically baroclinic type is wavelike in a finite region if $\omega > m\beta\sqrt{\lambda_1\lambda_2}/\Lambda$ and else evanescent. Other part of the spectrum is a discrete set of the segment $(-\infty, \inf\{m\bar{V}_2/r\})$, including asymptotically barotropic and baroclinic types without a critical layer.

6.3. *The decay of the asymptotically BT and BC modes*

The modal analysis above in §6.2 shows that the perturbation types belonging to the continuous spectrum are neutral, i.e., are maintained without growth or damping with time. However, it is known that treating the initial-value problem correctly shows that such modes may give rise to asymptotic alegbraic decay with time (Case 1960), or to algebraic growing (e.g. Burger 1966). Since the perturbation expressions in the complex ω-plane contain poles and branch cuts as is seen from (6.18) or (6.24), a natural question is what is their contribution to the flow stability properties. As is shown in this section, these types contribute to its stability by causing decaying rather than neutrality of a given initial perturbation.

Consider a time-dependent PV perturbation of azimuthal mode number m in the lower layer, $q_2(r,\theta,t) = \zeta_2(r,t)e^{im\theta}$. Its Laplace transform is defined as

$$\mathcal{Q}_2(r,\omega) = \int_0^\infty \zeta_2(r,t)e^{i\omega t}dt, \tag{6.27}$$

where the notation $\mathcal{Q}_i$ is in agreement with the definition (3.3). The inverse Laplace transform is given by

$$\zeta_2(r,t) = \frac{1}{2\pi}\int_{-\infty+i\gamma}^{\infty+i\gamma} \mathcal{Q}_2(r,\omega)e^{-i\omega t}d\omega, \tag{6.28}$$

where the Bromwich contour of integration is along $\mathrm{Im}(\omega) = \gamma$, where γ is greater than the imaginary part of all the singularities of $\mathcal{Q}_2(r,\omega)$.

Laplace transforming the linearized equation for q_2 in (3.2) gives

$$\left(\frac{\bar{V}_2}{r} - \frac{\omega}{m}\right)\mathcal{Q}_2 - \frac{\Phi_2}{r}\frac{d\bar{Q}_2}{dr} = \frac{\zeta_2(r,t=0)}{im} \tag{6.29}$$

Let us assume for simplicity that $\zeta_2(r,t=0) = \delta(r-r_0)/r$ and denote the solution to (6.29) in this case by $\chi(r,r_0;\omega)/r$; this solution is the response function of the system to

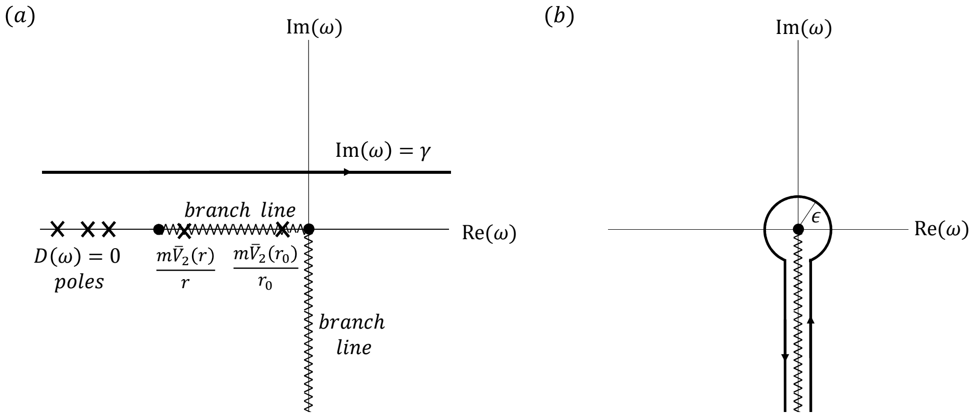

Figure 4: (a) Schematic drawing of the location on the complex ω-plane of the poles and branch lines of the Laplace transform response. There are poles due to the discrete spectrum (where $D(\omega) = 0$), a pole at $\omega = m\bar{V}_2(r_0)/r_0$, a pole at $\omega = m\bar{V}_2(r)/r$, a pole at $\omega = 0$ due to the asymptotically BC mode, a branch line at $\mathcal{S}_1$ and a branch line at $\mathrm{Im}(\omega) < 0$ due to the asymptotically BT mode. Also, the Bromwich contour $\mathrm{Im}(\omega) = \gamma$ is designated. (b) the contour for calculating the inverse Laplace transform of the asymptotically barotropic mode.

an initial delta function perturbation. Thus, the equation for $\chi(r; r_0, \omega)$ is

$$\left(\frac{\bar{V}_2}{r} - \frac{\omega}{m}\right)\chi(r; r_0, \omega) - \beta\int_{R_2}^{\infty}\frac{G_{22}(r, r')}{r'}\chi(r'; r_0, \omega)dr' = \delta(r - r_0). \tag{6.30}$$

Asymptotically at $r \to \infty$ the solutions to (6.30) coincide with the solutions to (6.1), which by §6.2 are asymptotically in the form of Hankel function of the first kind (see (6.18)) or Whittaker function (see (6.24)). Since for large ω, it is known that

$$H_{2m}^{(1)}\left(2\sqrt{\frac{m\beta r}{\omega}}\right) \sim \frac{1}{(2m)!}\left(\frac{m\beta r}{\omega}\right)^{2m}, W_{\kappa,m}\left(\frac{2\Lambda r}{\sqrt{\lambda_1\lambda_2}}\right) \sim r^{\frac{m\beta\lambda_1\sqrt{\lambda_1\lambda_2}}{2\Lambda\omega} - \frac{1}{2}}e^{-\frac{\Lambda r}{\lambda_1\lambda_2}} \tag{6.31}$$

(Abramowitz & Stegun 1964), then χ is bounded as $|\omega| \to \infty$. It is therefore possible to deform the Bromwich contour integral until it consists only of integrals around poles and cuts.

In Appendix E the poles of $\chi(r, r_0; \omega)/r$ are shown to be of four types: (i) a discrete isolated set corresponding to perturbation types with no critical layer, (ii) the point $\omega = \bar{V}_2(r_0)/r_0$, (iii) a branch cut along the segment $\mathcal{S}_1$, and (iv) the poles of the regular functions $\xi(r; r_0, \omega)$ defined by (E 3). Here we use the asymptotic (at $r \to \infty$) expressions for $\xi(r; r_0, \omega)$, which are identical to the asymptotic perturbations found in §6.2. Two types of singularities occur in the asymptotic regime: one is the singularity $1/\sqrt{\omega}$ that appears in (6.18), and the second is the singularity $1/\omega$ that appears in (6.24) (in the expression for κ). To account for the singularity $1/\sqrt{\omega}$ a branch of the square root must be chosen; for convenience we choose the branch cut to be on the negative imaginary axis. A schematic drawing illustrating the various poles and branch cut locations is given in figure 4a. The singularity at $\omega = 0$ and the branch cut of $\sqrt{\omega}$ are unique to the beta cone model.

The contribution of (i) to the inverse Laplace transform is a discrete sum of exponentials of the form $e^{-i\omega_n t}$, where $\{\omega_n\}$ is the discrete mentioned set. In the same way, the pole at $m\omega = \bar{V}_2(r_0)/r_0$ gives rise to a simple exponential $e^{-im\bar{V}_2(r_0)t/r_0}$. The contribution of the branch cut $\mathcal{S}_1$ results in algebraic decay as $1/t$ (Case 1960; Briggs *et al.* 1970).

To calculate the contribution of the barotropic mode to the integral, the contour of integration used is as shown in figure 4b. The integral along the small circle, $\int_0^{2\pi} H^{(1)}_{2m}\left(2\sqrt{m\beta r/\epsilon e^{i\phi}}\right) e^{-i\epsilon e^{i\phi}t} d\phi$, vanishes as $\epsilon \rightarrow 0$ (this can be found by direct numerical integration). Denoting the frequency by $\omega = ix$ along the negative imaginary axis, where x is real, the contribution to the integral (6.28) along the right side side of the branch cut is

$$\int_{-\infty}^{0} H^{(1)}_{2m}\left(2\sqrt{\frac{m\beta r}{ix}}\right) e^{-i\cdot ixt} dx = -\int_{0}^{\infty} H^{(1)}_{2m}\left(2\sqrt{\frac{m\beta r}{-ix}}\right) e^{-xt} dx. \tag{6.32}$$

Asymptotically at $t \rightarrow \infty$ significant contributions to the integral will come only from points x near zero. Therefore, the Hankel function in the integrand can be replaced by its asymptotic approximation at $x \sim 0$, which is

$$H^{(1)}_{2m}\left(2\sqrt{\frac{m\beta r}{-ix}}\right) \sim \left(\frac{-i}{m\pi^2 \beta r}\right)^{1/4} x^{1/4} \exp\left(2i\sqrt{\frac{m\beta r}{-ix}} - im\pi - \frac{i\pi}{4}\right). \tag{6.33}$$

(Abramowitz & Stegun 1964). Since the exponential term is bounded by 1, the integral in (6.32) is bounded by the following integral,

$$\left(\frac{1}{m\pi\beta r}\right)^{1/4} \int_0^\infty x^{1/4} e^{-xt} dx = \left(\frac{1}{m\pi\beta r}\right)^{1/4} t^{-5/4} \mathit{\Gamma}(5/4) \tag{6.34}$$

where $\mathit{\Gamma}$ is the gamma function. The integral over the other line gives an identical time dependence, so we conclude that the perturbation decays asymptotically as $t^{-5/4}$ in this case.

The contribution of the asymptotically baroclinic mode is simpler since there is only one singularity at $\omega = 0$ with no branch cuts. We assume that r is large enough so the asymptotic expansion of the Whittaker function can be used, $W_{\kappa,m}(r) \sim r^{\frac{\mathit{\Omega}}{\omega} - \frac{1}{2}} e^{-\frac{\mathit{\Lambda} r}{\lambda_1 \lambda_2}}$ (Whittaker & Watson 1996), where $\mathit{\Omega} = \frac{m\beta\lambda_1\sqrt{\lambda_1\lambda_2}}{2\mathit{\Lambda}}$. The inverse Laplace transform is then

$$\frac{1}{2\pi}\int_{-\infty+i\gamma}^{\infty+i\gamma} W_{\kappa,m}(r) d\omega \propto \frac{1}{2\pi}\int_{-\infty+i\gamma}^{\infty+i\gamma} r^{\frac{\mathit{\Omega}}{\omega}} e^{-i\omega t} d\omega = i\delta(t) + \frac{i\sqrt{i\mathit{\Omega}}}{\sqrt{t}} J_1\left(2\sqrt{|\mathit{\Omega}| t \ln r}\right), \tag{6.35}$$

where the last equality is from Bateman (1954). Since for large times $J_1(2\sqrt{|\mathit{\Omega}| t \ln r}) \sim t^{-1/4}\cos(2\sqrt{|\mathit{\Omega}| t \ln r} - 3\pi/4)$ (Abramowitz & Stegun 1964), the BC mode oscillates while its amplitude decays as $t^{-3/4}$.

7. Aspects of the CC and CT instabilities

7.1. *The CC instability*

In the contour-contour resonance the instability is due to the interaction of the PV waves at the liquid contours $r = R_1$ and $r = R_2$. In this case the bottom topography at $r > R_2$ can be neglected; this amounts to setting $\beta = 0$ where it appears explicitly in (4.9)-(4.11) (but not setting $\beta = 0$ in the expressions for PV discontinuities $\mathit{\Delta}_1$ and $\mathit{\Delta}_2$ in (4.2)). By (4.11), in this case η vanishes; a system of two homogeneous algebraic equations for α_1 and α_2 is established. This system can be written in matrix form,

$$\begin{bmatrix} M_{11} - \frac{\omega}{m} & M_{12} \\ M_{21} & M_{22} - \frac{\omega}{m} \end{bmatrix} \begin{bmatrix} \alpha_1 \\ \alpha_2 \end{bmatrix} = \begin{bmatrix} 0 \\ 0 \end{bmatrix}, \tag{7.1}$$

where

$$M_{11} = \frac{\bar{V}_1(R_1) - \mathit{\Delta}_1 G_{11}(R_1, R_1)}{R_1}, \quad M_{12} = -\frac{\mathit{\Delta}_1 G_{12}(R_1, R_2)}{R_2}, \tag{7.2}$$

$$M_{21} = -\frac{\mathit{\Delta}_2 G_{21}(R_2, R_1)}{R_1}, \quad M_{22} = \frac{\bar{V}_2(R_2) - \mathit{\Delta}_2 G_{22}(R_2, R_2)}{R_2}. \tag{7.3}$$

In order to have a nontrivial solution, the determinant of the 2×2 matrix in (7.1) should be zero. This yields the eigenvalue equation, which is quadratic in ω,

$$\frac{\omega^2}{m^2} - (M_{11} + M_{22})\frac{\omega}{m} + M_{11}M_{22} - M_{12}M_{21} = 0, \tag{7.4}$$

from which we get the dispersion relation for the two-contours subsystem,

$$\omega_{A,B} = \frac{m}{2}\left[(M_{11} + M_{22}) \pm \sqrt{(M_{11} + M_{22})^2 - 4(M_{11}M_{22} - M_{12}M_{21})}\right]. \tag{7.5}$$

The subscript A or B corresponds to applying + or − sign before the square root in (7.5), respectively. The two eigenvectors corresponding to the two eigenvalues in (7.5) are the two modes of PV perturbations at the liquid contours, which we accordingly call type A or type B; they are connected to the contours' deformations via (4.6) (see Kizner *et al.* 2013; Rabinovich *et al.* 2018).

Figure 5 shows an example how the CC instability can be recognized via the dispersion curves $\omega(m)$. The basic flow parameters are $R_1 = R_2 = 2.5, \mathit{\Gamma}_1 = -1, \lambda_1 = \lambda_2 = 1/2$; this setup is called for future reference configuration A of the flow. The eigenvalues of the isolated CC system are calculated via (7.5), while the eigenvalues of the full system are calculated numerically as explained in §4.2. For easier tracking of the dispersion relation, we calculate the dispersion curves for continuously varying m and mark the points corresponding to integer m, which are the physically relevant values (see (3.3)). Figure 5a shows the angular phase velocity of the perturbations, $\mathrm{Im}(\omega)/m$, vs. the wavenumber m, for the two CC waves and the unstable perturbation. When $m = 3, 4$ or 5 the two phase velocities of the two CC waves coincide and CC instability occurs, as can be seen from the growth rate ($\mathrm{Im}(\omega)$) curve in figure 5b.

At $m = 6$ the angular velocities of the two CC waves are different, therefore there cannot be a CC instability. However, since the flow is still unstable at $m = 6$ (the growth rate is nonzero), the conclusion is that one of the CC waves resonates with the topographic perturbations at $r > R_2$ (since the outer region at $r > R_2$ by itself is always stable, see §6).

In case of a CC instability, the growth rate of the full system g_F can be compared to that found using the isolated CC system, g_{CC}. In the case shown in figure 5b, at the low mode numbers ($m = 3$ or $m = 4$) the inequality $g_F \leqslant g_{CC}$ holds; therefore, at these mode numbers the topography outside causes a reduction in the growth rate. At $m = 6$ the inequality is inversed, $g_F > g_{CC} = 0$; the topography at $r > R_2$ then destabilizes the flow, since without it the flow would stay stable. This result is not specific to the particular parameters of the flow in this example, and was observed in all our calculations: at low mode numbers the CC resonance is dominant, yet the full-system growth rate is lower than expected due to the CC interaction alone. Also, at larger mode numbers the CT resonance becomes the only one that contributes to instability while the CC subsystem is stable. Another example for this result is given below.

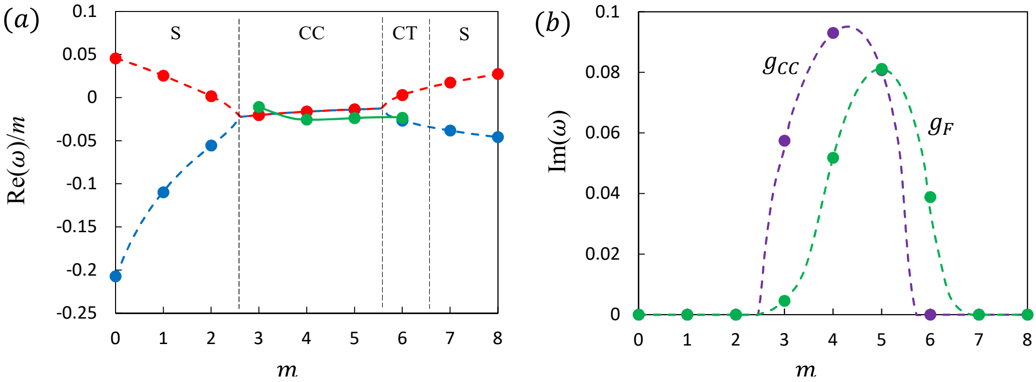

Figure 5: Real and imaginary parts of the eigenvalues for CC and full resonance. The basic flow parameters are $R_1 = 2.5, R_2 = 2.5, \mathit{\Gamma}_1 = -1$, $\beta = -0.5$ (configuration A). (a) Perturbation angular velocity Re(ω) vs. the mode number m. The angular velocities of two CC waves are given by red and blue dotted lines, and that of the full system is given by green whenever there is instability. Points with physically relevant values of m (integers) are marked. S, CC and CT designate regions where the flow is stable, unstable due to CC resonance, unstable due to CT resonance, accordingly. (b) The growth rate Im(ω) vs. the mode number for the CC resonance (g_{CC}, purple) and for the full system (g_F, green). The points are joined by straight lines for better visualization.

7.2. *The CT instability*

As is shown in figure 5, the unstable $m = 6$ mode, which is not caused by CC resonance, has a real angular velocity very close to one of the CC-interaction modes. This suggests that actually the CC perturbation type B, having the lowest angular velocity of the two (see (7.5)), is the one that resonates with the topographic perturbations at $r > R_2$. In order to identify the resonating perturbation type in the CC system by the integral eigenvalue approach, we rewrite the eigenvalue equations (4.9)-(4.11) in a way that the CC perturbation types appear decoupled; the calculation is given in Appendix F. This procedure can be viewed as partial diagonalization of the system of equations (4.9)-(4.10) by moving to the CC eigenmodes coordinates; the resulting equations (G 5)-(G 7) in Appendix F are diagonal in the isolated CC system (i.e. in case that there is no topography outside the contours). It is found that, in case of CCT instability, only type B resonates with the topographic perturbations.

To understand why type B is the one that resonates with the topographic perturbations, we apply pseudo-momentum considerations. Recall that two modes may resonate only if their pseudomomenta are opposite in sign (§5.1). Since the topographic types have positive pseudomomentum (see (5.4)), only the type having negative pseudomomentum can resonate with them. In appendix F it is proved that the pseudomomentum of a perturbation has the same sign as the slope of the dispersion curve (when m may be taken to vary smoothly); similar result was proven for the rotating shallow water (one layer, zonal) case by Iga (1999*b*). From figure 5a, it is clear that at $m = 6$ only type B has the negative pseudomomentum since only its dispersion curve is decreasing with m at $m = 6$.

As is shown in figure 2b, a flow with parameters $R_1 = 5, R_2 = 2, \mathit{\Gamma}_1 = -1, \lambda_1 = \lambda_2 = 0.5$ (we denote this flow configuration by B) is unstable to mode $m = 2$ perturbations, where the instability is CT instability. Figure 6 shows that in this case $m = 2$ is the gravest

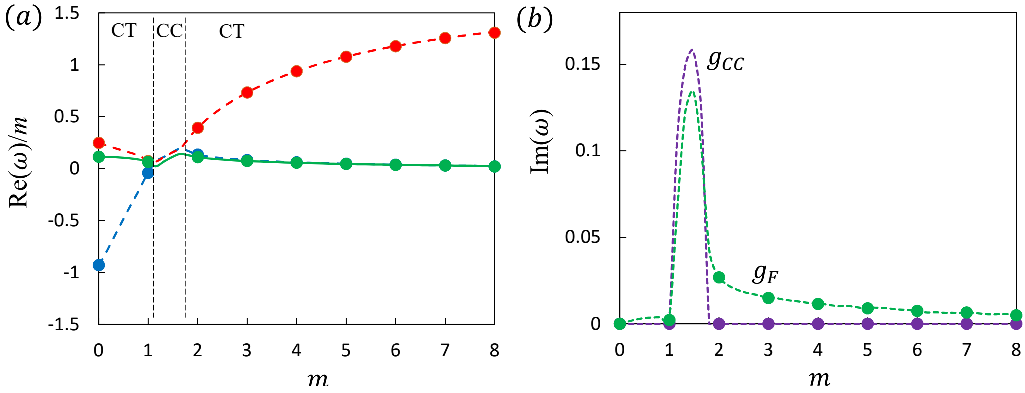

Figure 6: Real and imaginary parts of the eigenvalues for CC and full resonance. The basic flow parameters are $R_1 = 5, R_2 = 2, \mathit{\Gamma}_1 = -1$, $\beta = -0.1$ (configuration B). (a) Perturbation angular velocity $\mathrm{Re}(\omega)$ vs. the mode number m. (b) The growth rate $\mathrm{Im}(\omega)$ vs. the mode number for the full system. Notations and colors as in figure 5.

unstable mode. Again, the full-system phase velocity is close to that of perturbation type B of the CC subsystem; this is in accordance with its decreasing dispersion curve, pointing the fact that it bears negative pseudomomentum (Appendix F).

Figure 7 shows the growth rates of different mode numbers as functions of the radius of the lower ring, R_2, for the basic flow parameters $R_1 = 5, \lambda_1 = \lambda_2 = 0.5$ and $\beta = -0.1$. When $\mathit{\Gamma}_1 = 1$ (figure 7a) the lines of the $m \geqslant 2$ modes are composed of two 'bulges' that get close to each other with increasing mode number till their merging at $m = 8$. The instability in these 'bulge' regime is of type CC, as was shown for the $m = 2$ case in figure 2a. At the left side of each of the lines, it becomes nearly horizontal; in this range the instability is of type $\mathrm{C_2T}$ (this was also shown for the $m = 2$ case in figure 2a). Between these two regions the instability is of type CCT. Mode $m = 1$, contrary to the other modes, is unstable only due to CC resonance.

Similarly, when $\mathit{\Gamma} = -1$ (figure 7b), the lines of the growth rates at $m \geqslant 2$ modes can be seen as composed of three parts: one is the low-R_2 regime, where the lines are nearly horizontal, and then the instability is of type $\mathrm{C_1T}$. The CC instability part consists of the line where steep increase in growth rate begins (going from left to right). Between these two regions the instability is of type CCT; this was also shown for the $m = 2$ case in figure 2b. Again, mode $m = 1$ is unstable only due to CC resonance.

7.3. *Barotropic and baroclinic CT resonance*

Another useful property of the eigenvalue equations in integral form, (4.9)-(4.11), is the simple separation of barotropic and baroclinic couplings. By equations (3.15)-(3.18), the Green functions G_{11}, G_{12}, G_{21} and G_{22} are linear combinations of the two more basic, baroclinic and barotropic Green functions, G_{BT} and G_{BC}. The latter serve as the coupling coefficients between the contours' perturbations α_1 and α_2 to the perturbation outside, η. Therefore, if we set $G_{BT} \equiv 0$ ($G_{BC} \equiv 0$) in the integral terms in (4.9)-(4.11), only baroclinic (barotropic) couplings to the outside perturbation are allowed. On comparing the resulting growth rates in any case we can identify which of the couplings is dominant. When the BT (BC) coupling is dominant, the contours are resonating with the

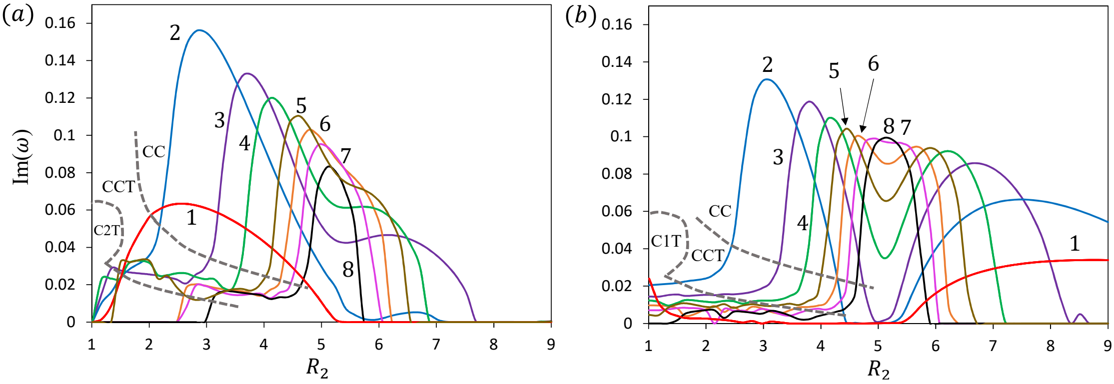

Figure 7: Growth rates $\mathrm{Im}(\omega)$ for different mode numbers as functions of R_2 at $R_1 = 5, \beta = -0.1, \varLambda = 1$, and $\lambda_1 = \lambda_2 = 0.5$ for (a) $\varGamma_1 = 1$, (b) $\varGamma_1 = -1$. The mode numbers are labeled next to each curve.

asymptotically BT (BC) mode. If they are both dominant, the contours are resonating with a mixed mode.

It was found that in most cases the barotropic CT resonance is the dominant one, while the baroclinic CT resonance is very weak or absent. An example of the growth rates of the full system, the CC subsystem, the BT coupling and the BC coupling is shown in figure 8a; the relative thickness of the upper layer, λ_1, is varied. In this case $R_1 = 5, R_2 = 2, \varGamma_1 = -1, \beta = -0.1$ and the mode number is $m = 2$. In this case the instability is of type CCT (see figure 2b), and type-B perturbation of the CC subsystem resonates with the BT perturbation type whenever instability occurs.

An example for a configuration where the baroclinic coupling is the dominant one is not easily found. The reason is that for all r and r' the inequality $G_{BC}(r, r') < G_{BT}(r, r')$ holds, as is verified directly from equations (B 6) and (B 12); moreover, if $|r - r'| \gg r$ this inequality gets stronger, $G_{BC}(r, r') \ll G_{BT}(r, r')$. Therefore, the baroclinic interaction terms are usually negligible compared to the barotropic terms. The growth rates and the eigenfunctions are, accordingly, determined mainly by the barotropic couplings. This explains the barotropic governor effect, in which barotropic shear leads to reduction in baroclinic growth rate (James 1987). In the case of circularly symmetric flow, Solodoch *et al.* (2016) noted that this effect may be attributed to the barotropic strain rather than shear, but anyway both the shear $\partial\bar{V}_2/\partial r$ and strain $r\partial(\bar{V}_2/r)/\partial r$ are nonzero in our case.

The only way to find an example where the baroclinic CT resonance is dominant is to look at configurations where the barotropic growth rates are close to zero. In this way, the subsystem with only barotropic couplings can be viewed as almost stable, while the baroclinic couplings can be viewed as small perturbation; these can affect the resulting eigenvalues of the full system. Such an example, where $R_1 = R_2 = 5, \varGamma_1 = 1$ and $\beta = -0.1$, is shown in figure 8b. In the range $0.123 \leqslant \lambda_1 \leqslant 0.15$ the instability is of type C_2T, and then the growth rate of the full system g_F is very close to that due to the BC coupling, g_{BC}.

As λ_1 approaches 1 (i.e. the lower layer becomes very thin) the BC coupling becomes dominant (figure fig:8b). This is consistent with the findings of Ribstein & Zeitlin (2013) (who investigated two-layer shallow water with bottom topography), that when the depth of the lower layer decreases, the baroclinic instability overtakes the barotropic instability.

In terms of the resonating perturbations, however, this range of $\lambda_1 \approx 1$ cannot be attributed to instability with the baroclinic perturbation type, since the instability is CC there (as $g_{CC} \neq 0$); the baroclinic interaction only contributes to increasing of the growth rate, not to its origin.

7.4. *Resonance with the continuous spectrum*

Examples of three unstable solutions (found numerically) for η are shown in figure 9 for three configurations of the basic flow. For configuration A (see §7.1 and figure 5) the basic flow profiles are shown in figure 9a, and the amplitude and relative phase of the resulting unstable perturbation are shown in figures 9d and 9g, respectively; since $\omega_r = \mathrm{Re}(\omega) < 0$ in this case while $\bar{V}_2 \geqslant 0$, this cannot be a critical layer instability. The instability is of type CC and the growing perturbation outside is reminiscent of the asymptotically BT mode (6.20); due to the fact that ω is complex, the alternating PV profile is subject to exponential decrease with r (for details see Rabinovich *et al.* (2019)).

The PV and velocity profiles of configuration B (see §7.1 and figure 6) are shown in figure 9b. As shown above, for this configuration the instability is of type CCT, and since $\omega_r \in \mathcal{S}_1$, this is a critical layer instability. The unstable perturbation (figure 9e) is reminiscent of the critical layer structure (§4); this can be most clearly viewed by the rapid change in the relative phase of the perturbations in a thin range near $r_c = m(\bar{V}_2/r)^{-1}(\omega_r)$ (figure 9h).

The third configuration, which we label configuration C, corresponds to a case where the instability is of type $\mathrm{C_2T}$ and the baroclinic coupling is dominant. The flow parameters are $R_1 = R_2 = 5, \mathit{\Gamma}_1 = 1, \beta = -0.1, \lambda_1 = 0.14$ ans $\lambda_2 = 0.86$; from figure 8 the dominance of the baroclinic coupling is evident. The unstable perturbation (figures 9f,i) are reminiscent of the critical layer structure near r_c (at about 5.1), and at $r > r_c$ it is reminiscent of the stable BC mode.

To understand the structure of the solutions in the case of CT instability we approximate the solution to the eigenvalue equations when the growth rates are small. The integral equation (4.11) is nonsingular and $\eta(r)$ is then given by (6.5) with no delta function and without need for the principal value calculation, i.e.

$$\eta(r) = \frac{\xi(r)}{\frac{\bar{V}_2}{r} - \frac{\omega}{m}}. \tag{7.6}$$

Plugging (7.6) into (4.11) yields the following equation for ξ,

$$-\frac{G_{21}(r,R_1)}{R_1}\alpha_1 - \frac{G_{22}(r,R_2)}{R_2}\alpha_2 + \xi(r) = \int_{R_2}^{\infty} \frac{\beta G_{22}(r,r')}{\frac{\bar{V}_2(r)}{r} - \frac{\omega}{m}}\xi(r')dr'. \tag{7.7}$$

We denote $\omega = \omega_r + i\omega_r$, where ω_r and ω_i are the real and imaginary parts of ω, respectively. If ω is near bifurcation, i.e., ω_i is small, we may assume that $\mathrm{Im}\xi$ is also small. By (3.3) the expression for the PV perturbation at $r > R_2$ is

$$q_2(r,\theta,t) = -\frac{\beta}{r}\frac{\mathrm{Re}[\xi(r)](\frac{\bar{V}_2}{r} - \frac{\omega_r}{m})}{(\frac{\bar{V}_2}{r} - \frac{\omega_r}{m})^2 + \frac{\omega_i^2}{m^2}} e^{\omega_i t}\cos(m\theta - \omega t), \tag{7.8}$$

where the term $\mathrm{Im}[\xi(r)]\omega_i$ was neglected being of second order in ω_i. The solution vanishes at $r = m\bar{V}_2/\omega_r$ and switches the sign of PV between the two sides; the similarity to a critical layer structure is more prominent as the ration ω_i/ω_r becomes small.

For the basic flow in figures 9b and 9c this ratio is, accordingly, $\omega_i/\omega_r \approx 0.128$ and $\omega_i/\omega_r \approx 0.1$. By (7.8), as $\omega_i \to 0$, the zone of switching PV signs in the unstable mode becomes more narrow; thus in the limit of $\omega_i \to 0$ the discontinuous nature of the critical

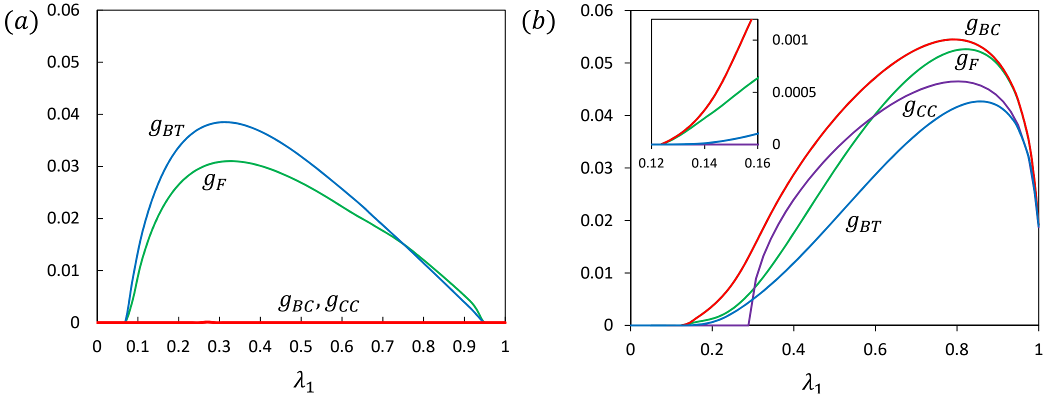

Figure 8: Growth rates $\mathrm{Im}(\omega)$ for different resonances as functions of λ_1 for (a) $R_1 = 5, R_2 = 2, \Gamma_1 = -1$, $\beta = -0.1$ and $m = 2$, (b) $R_1 = R_2 = 5, \Gamma_1 = 1$, $\beta = -0.1$, $m = 2$. The resonance types are labeled next to each curve. Inset in the upper-left corner on (b) represents the growth rates in the range $0.12 < \lambda_1 < 0.16$.

layer is restored. In the approximation of linear perturbations, equation (7.8) describes a thin layer having an m-fold symmetry centered at $r = m\bar{V}_2/\omega_r$, and which becomes stronger and broader with time.

In the case of CT resonance, part of the eigenmodes in the outer region $r > R_2$ constitute a continuum (§6). This suggests that the resonance in this case is with a collection of the perturbations of the continuous spectra, as was shown by Iga (1999*a*). A simple explanation to this fact may be given on grounds of pseudomomentum considerations: the pseudomomentum of the resonating perturbations in the system must cancel to zero (see §5.1). Since the pseudomomentum of the contours is always finite (the first two terms in (5.4)), the pseudomomentum of the topographic perturbation outside must also be finite. But the pseudomomentum of one critical-layer perturbation (the third term in (5.4)) is infinite (by (6.5)); therefore in order to have a finite-pseudomomentum topographic perturbation, it must be composed of collection of critical-layer perturbations such that the third term in (5.4) is finite.

Following Iga (1999*a*), to determine the structure of this collection, we use projections. The unstable outer PV perturbation in the lower layer, $\eta_\omega(r)$ (where $\mathrm{Im}(\omega) > 0$), is projected on the possible stable self-excitations of the outer region discussed in §4, $\eta_{\omega'}$ (ω' being real, and the critical layer is at $r_c = (V_2/r)^{-1}(\omega'/m)$). Since the stable solutions constitute an orthonormal set (see §4.1), the projection $\langle \eta_\omega, \eta_{\omega'} \rangle$ correctly calculates the weights in this collection. By (6.5) we get

$$\begin{aligned}\langle \eta_\omega, \eta_{\omega'} \rangle &= \int_{R_2}^{\infty} \eta_\omega(r) \left[D(\omega')\delta\left(\frac{\bar{V}_2(r)}{r} - \frac{\omega'}{m}\right) + P\frac{\xi^*_{\omega'}(r)}{\frac{\bar{V}_2}{r} - \frac{\omega'}{m}} \right] dr \\ &= \frac{D(\omega')}{|(\bar{V}_2/r)'_{r_c}|}\eta_\omega(r_c(\omega')) + P\int_{R_2}^{\infty} \frac{\xi_\omega(r)\xi^*_{\omega'}(r)dr}{(\frac{\bar{V}_2}{r} - \frac{\omega}{m})(\frac{\bar{V}_2}{r} - \frac{\omega'}{m})} \\ &\approx \frac{D(\omega')}{|(\bar{V}_2/r)'_{r_c(\omega')}|}\eta_\omega(r_c(\omega')) - \frac{i\pi}{|(\bar{V}_2/r)'_{r_c(\omega')}|}\eta_\omega(r_c(\omega'))\xi^*_{\omega'}(r_c(\omega')).\end{aligned} \tag{7.9}$$

The principal value integral was calculated via Cauchy's integral theorem (see e.g. Killingbeck 2012) using the fact that $\omega_i > 0$ for an unstable mode, and assuming that the

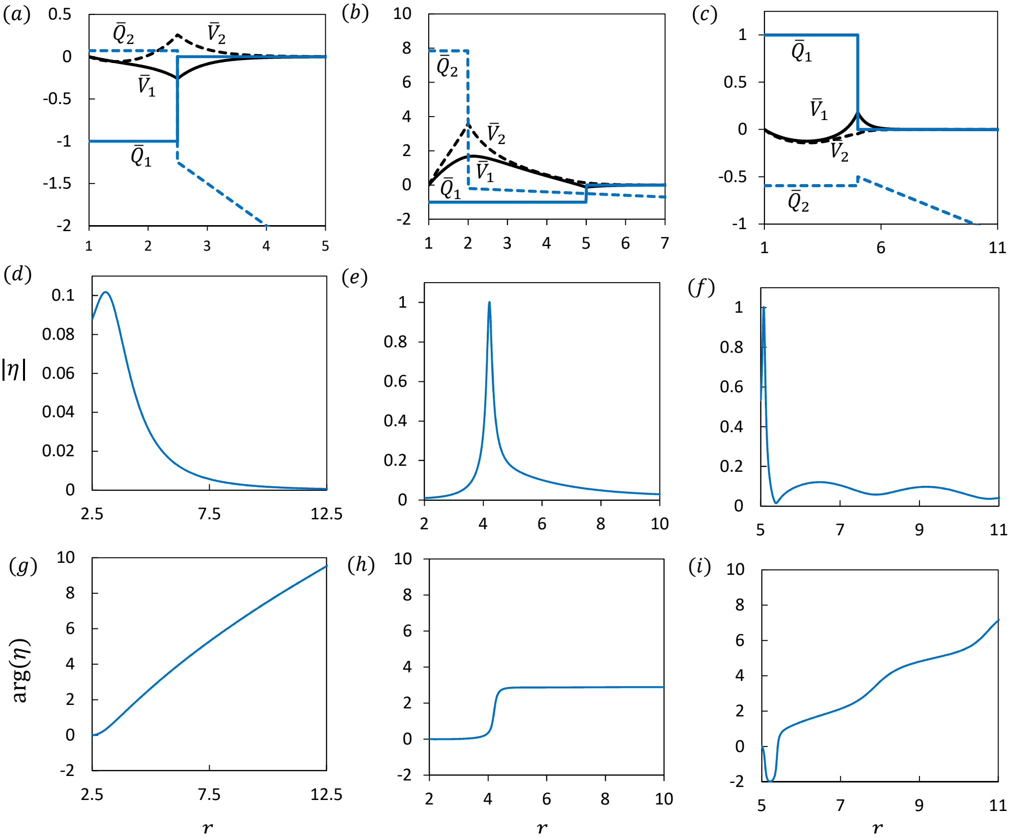

Figure 9: Examples of profiles of the basic flow ((a)-(c)) and the corresponding unstable PV perturbations amplitude ((d)-(f)) and relative phases ((g)-(i)). The basic flow parameters for each triple are: (a)+(d)+(g) $R_1 = R_2 = 2.5, \mathit{\Gamma}_1 = -1, \beta = -0.5, \lambda_1 = \lambda_2 = 0.5$ (configuration A), where $m = 5$ is the gravest mode with frequency $\omega = -0.118 + 0.081i$. (b)+(e)+(h) $R_1 = 5, R_2 = 2, \mathit{\Gamma}_1 = -1, \beta = -0.1, \lambda_1 = \lambda_2 = 0.5$ (configuration B), where $m = 2$ is the gravest mode with frequency $\omega = 0.221 + 0.027i$. (c)+(f)+(i) $R_1 = R_2 = 5, \mathit{\Gamma}_1 = 1, \beta = -0.1, \lambda_1 = 0.2, \lambda_2 = 0.8$ (configuration C), where $m = 2$ is the gravest mode with frequency $\omega = -0.0097 + 0.0002i$. Notations and colors of figures (a)-(c) as in figure 1. In figures (d)-(f) the PV perturbations in the upper layer are denoted by solid blue line and in the lower layer by dotted blue line. Arrows denote delta functions, their height corresponds to the multiplicative factor in front of the delta functions.

main contribution to the integral is near the critical layer. We assume that the changes in $D(\omega'), \xi_{\omega'}(r_c(\omega'))$ and $\bar{V}_2(r_c(\omega'))$ with ω' are small relative to changes in $\eta_\omega(r_c(\omega'))$; the weight then goes as

$$|\langle\eta_\omega, \eta_{\omega'}\rangle|^{1/2} \sim |\eta_\omega(r_c(\omega'))|^{1/2} = \left[\frac{|\xi_\omega(r_c(\omega'))|}{(\omega' - \omega_r)^2 + \omega_i^2}\right]^{1/2}. \tag{7.10}$$

If $\xi_\omega(r_c(\omega'))$ changes slowly enough with ω' then the expression in (7.10) is maximized at $\omega' = \omega_r$; this means that the resonating eigenfunctions are those with frequencies closed to ω_r. Figure 10 shows that the approximation (7.10) is in excellent agreement with the direct calculation of the weight. Approximating (7.10) further by assuming that the nominator is constant leads to

$$|\langle \eta_\omega, \eta_{\omega'} \rangle|^{1/2} \sim \left[\frac{1}{(\omega' - \omega_r)^2 + \omega_i^2} \right]^{1/2}, \tag{7.11}$$

as obtained by Iga (1997) in the one-layer, zonal, rotating shallow water model. This expression, however, is not a good approximation for frequencies outside the immediate neighborhood of ω_r as shown in figure 10.

8. Nonlinear evolution of CC vs. CT instabilities

According to the linear stability analysis scheme, at first glance it seems that there shouldn't be any substantial difference between the evolution of the flow in case of CC instability to that of CT instability. After all, the source of the instability brings the entire system to collectively rotate and grow; the linear-stability analysis unstable solutions are written as if the phase locking is achieved immediately. However, in practice, the phase-locking is an evolving effect (see e.g. Rabinovich *et al.* (2019)). If the system is subject to some random noise, the first two parts to phase-lock are the resonating perturbation types. Therefore, with time they become the dominant growing perturbations, where the rest of the perturbations are influenced by the first ones. The subsystem that resonates reaches large-scale perturbations first, and consequently nonlinear effects become pronounced first for this subsystem.

We conduct high-Reynolds-number simulations employing the coefficient-form partial differential equation package of the COMSOL software based on the finite-element method, see Rabinovich *et al.* (2019) for details. The vorticity-diffusion term $\nu\nabla^2 Q_i$ is added to the right-hand side part of equations (2.5) in order to maintain numerical stability. The resulting coupled system composed of equations (2.4) and the equation of PV evolution (i.e. equation (2.5) supplemented with the diffusion term) is solved as an initial-value problem in a two-dimensional (r, θ) rectangular grid, $1 < r < 30$ and $0 \leqslant \theta \leqslant 2\pi$. The unknown variables are the streamfunction and the PVs. We apply the periodicity conditions at $\theta = 0$ and $\theta = 2\pi$ and the no-slip conditions at both radial boundaries by setting $\partial\Psi_i/\partial r = \partial\Psi_i/\partial\theta = 0$ at $r = 30$, and $\partial\Psi_i/\partial r = 0$ and $\Psi_i = 0$ at $r = 1$.

The computational domain, $30 \times 2\pi$ in size, is divided into three subdomains. The first, fine-grid domain, $1 \leqslant r < 1.5$ with the mesh size of 0.05×0.03, is set off in order to be able to resolve the viscous boundary layer that may form next to the cylinder. The second is the main domain $1.5 \leqslant r < 20$ with the mesh size of 0.1×0.03. In both domains, ν is set to be 0.0001. The third domain, $20 \leqslant r \leqslant 30$, is set off as an absorbing layer to prevent reflections. In order to get a reasonable machine time for the evolution of linear instability of the flow, we add a random perturbation to the basic PV field in the form of Gaussian noise on the entire computational grid. More details on the method used can be found in Rabinovich *et al.* (2019).

8.1. *CC instability*

An example of the evolution of an unstable flow in case of a CC instability is shown in figure (11). The flow parameters are the same as in figures 5 and 9a, namely, $R_1 = 2.5, R_2 = 2.5, \varGamma_1 = -1$ and $\beta = -0.5$. As is shown in figure 5b, the gravest unstable mode is $m = 5$, and indeed this is the mode that evolved most rapidly in the simulation. At first, the deformation of the contours is seen at $t = 30$; the upper contour is tilted relative to the

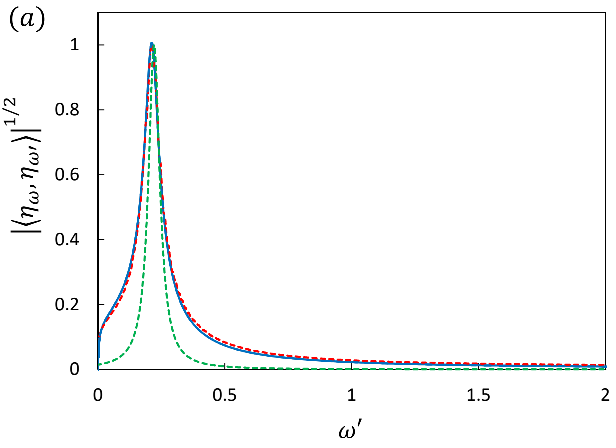

Figure 10: Amplitude of the spectrum of the PV perturbation in the lower layer at $r > R_2$ (blue solid line), the approximated expression (7.10) (red dotted line) and the approximated expression (7.11) (green dotted line) for $R_1 = 5, R_2 = 2, \Gamma_1 = -1, \beta = -0.1$ (configuration B).

lower one, they are phase-locked and propagate in the clockwise direction in accordance with the calculated frequency of the linear stability analysis, $\omega = -0.118 + 0.081i$.

As is shown at $t = 60$ and $t = 80$, the perturbations of the contours excite the perturbation types outside in the form of waves, which are similar to the stationary waves found in §6.2. Since the baroclinic wave mode decreases exponentially with distance, the dominant wave is the barotropic one, which decreases as $r^{-1/4}$. This barotropic mode has the form of spirals as was shown for barotropic flows on the beta cone (Rabinovich *et al.* 2019). These linear waves appear only in the lower layer, where the gradient of the basic PV exists.

During the nonlinear growing of the deformation, five couples of partially overlapping negative (in the upper layer) and positive (in the lower layer) PV patches can be identified (most clearly at $t = 60$). These can be viewed as modons, i.e. QG baroclinic vortical dipoles (e.g. Flierl *et al.* 1980; Kizner 1984, 1997). For each couple, the positive part stays attached to the cylinder, while the negative part is released and moves more freely (as can be seen from time $t = 160$ and on). At first ($t = 90$) each couple is created such that its propagation aims towards the cylinder; this causes the positive patch to deform and get close to the cylinder. Then the positive patch switches partner and the dipole moves outwards again ($t = 120$). Upon reaching a maximal distance from the island, the modons swing ($t = 160$) and returns back to the cylinder. Then the modons collide, exchange their partners, and new modons emerge. Due to wave radiation, dissipation and filamentation, this time the maximal distance from the cylinder is smaller. This process repeats in quasi-periodic manner in a similar fashion to the barotropic evolution shown by Rabinovich *et al.* (2019). At $t = 230$ the 5-fold symmetry is lost, two of the positive parts in the upper layer leave the cylinder and the five modons are wandering around.

The evolution in this case of CC instability is very similar to evolution of unstable barotropic flows on the beta-cone studied by Rabinovich *et al.* (2019), the main features of the QG evolution are: emergence of modons (instead of dipoles in the barotropic case) having a tendency to move counterclockwise, appearance of spiral barotropic PV

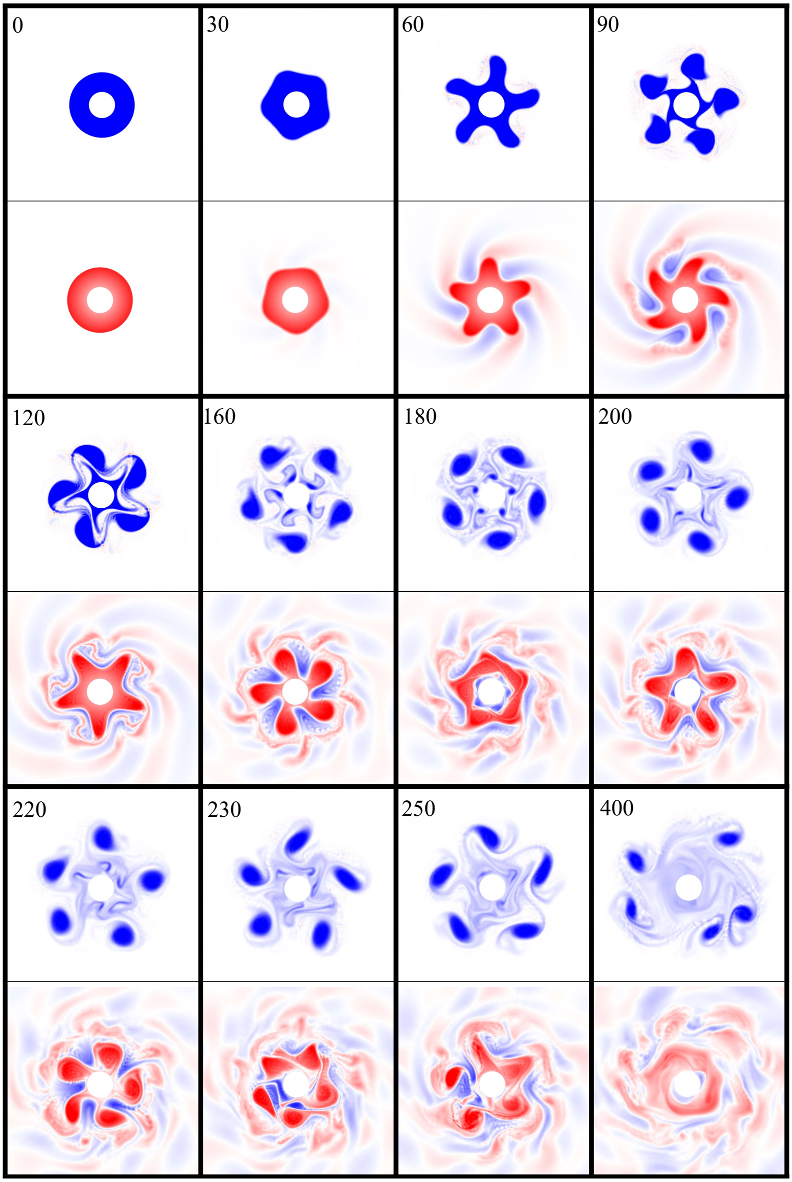

Figure 11: Evolution of the relative PV field in the upper layer (upper panel in each cuple) and the lower layer (lower panel). The basic flow parametrs are $R_1 = R_2 = 2.5, \Gamma_1 = -1, \beta = -0.1$ and $\lambda_1 = \lambda_2 = 0.5$ (configuration A); mode 5 is most unstable. Red/blue colours mark positive/negative PV; grey, the island. Time is specified in non-dimensional units at the upper-left corner of the upper panel in each couple.

waves propagating clockwise, quasi-periodic outward and inward motion of the modons with exchanging partners every cycle. The 'averaged' beta in this system can be defined according to the weight of each layer as $\lambda_1 \cdot 0 + \lambda_2 \cdot \beta = \lambda_2 \beta$, so it is -0.25 for the evolution in figure 11. As expected and as was found in simulations (not shown), at lower —β—

the maximal distance of the modons is larger, while at stronger $|\beta|$ new flow patterns are formed without emergence of modons.

8.2. *CT instability*

While the CC instability results in flow evolutions which are analogous to that in the barotropic case, the CT instability is rather different. The main reason is that now the dominant interaction is between one of the contours and a perturbation at $r > R_2$. This perturbation is reminiscent of the critical layer solution as shown in §7.4, so the contour resonates with a thin layer having alternating PV signs located at some distance from it. The resonating parts are the ones having the greatest amplitude of PV perturbation and therefore are the first to reach a nonlinear saturation during the phase-locking stage (cf. Rabinovich *et al.* 2019).

Evolution of CCT instability is shown in figure 12. The flow is in configuration B, as in figure 6 and 9b, where $R_1 = 5, R_2 = 2, \Gamma_1 = -1$ and $\beta = -0.1$. The resonance is between type-B perturbation of the CC subsystem and the topographic perturbations at $r > R_2$. As shown in figure 7b, the CCT instability in this configuration is close to the $\mathrm{C_1}$T-instability regime, and therefore in the mutual deformation of the contours, the significant deformation occurs at C_1 (t=30); minor deformations are seen in C_2. A narrow PV ring, having an $m = 2$ symmetry, is formed at $r \approx 4.2$ by $t = 30$; this ring is the collection of critical-layer perturbations having critical layers in the vicinity of $r = 4.2$ (§7.4).

Out of the initial random perturbations that were inserted into the system, only the resonant ones start to phase-lock and grow with time. Therefore the C_1 deformation and the new thin PV ring are the first to grow significantly in this case and reach large-scale perturbations, where nonlinearity becomes important. Due to nonlinear effects, the linear growing stops and the thin ring rearranges in the configuration shown at $t = 90$. This stop is the reason that no dipolar modons are emerged, contrary to the CC-instability case (§8.1), where both contours are deformed significantly.

During the times $t = 90$ to $t = 230$ the flow rotates counterclockwise and completes about three revolutions in a quasi-stationary manner. This structure is a baroclinic version of the tripolar structure found in the barotropic beta-cone model (Rabinovich *et al.* 2019, figure 14). It is reminiscent of stationary two-layer QG tripole vortices found numerically on the f-plane (Corread & Carton 1999; Sokolovskiy & Verron 2000) and that was investigated also on the beta plane (Kizner *et al.* 2017).

The tripole eventually breaks into two modon quartets ($t = 260$) composed of two PV patches at each layer. In the upper layer the PVs of the circle and its adjacent patch are equal, approximately -1, as was initially. In the lower layer the PVs are different since only the PV of the circular patch was there initially, its value being approximately 8.32; the PV of the adjacent patch, which has emerged from the interaction with the upper layer PV, is 0.3 on average. Since the positive PV circular core at the lower layer is so strong and only the non-circular patch in the upper layer is tilted vertically relative to it, this quartet behaves effectively as dipolar modon (composed of the circular positive vortex in the lower layer and non-circular vortex patch in the upper layer). Therefore after reaching a maximal distance of about 2.8 from the island ($t = 260$), the modon swings and comes back to the cylinder ($t = 294$).

9. Conclusion

We have investigated the possible resonances leading to instability of two layer QG circular flows around an island with the sea bottom sloping offshore ($\beta < 0$). The flow

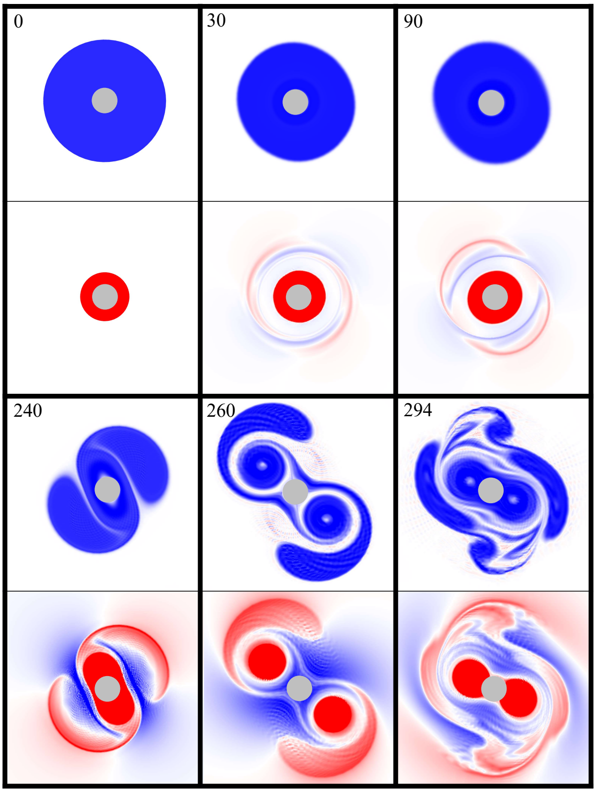

Figure 12: Evolution of the relative PV field in the upper layer (upper panel in each cuple) and the lower layer (lower panel). The basic flow parametrs are $R_1 = 5, R_2 = 2, \mathit{\Gamma}_1 = -1, \beta = -0.1$ and $\lambda_1 = \lambda_2 = 0.5$ (configuration B); mode 2 is most unstable. Colors and notations as in figure 11.

in each layer is composed of one uniform relative PV ring: the outer radius of the upper (lower) ring is R_1 (R_2) and the nondimensional PV inside it is $\mathit{\Gamma}_1 = +1$ or -1 ($\mathit{\Gamma}_2$, given by (4.3)). The azimuthal normal-mode analysis leads to a set of integral eigenvalue equations which have direct physical interpretation in terms of the possible resonances of the system.

The possible topographic PV perturbations exist only in the lower layer at $r > R_2$, where a nonzero PV gradient occurs. A continuous set of possible perturbations consists of those having a critical layer. Asymptotically at $r \to \infty$ these solutions split to two kinds, barotropic or baroclinic modes. When these modes rotate clockwise, they are wavelike in the radial direction and therefore on the two-dimensional plane a pattern of spiral PV patches appear. Both modes, although seem to be neutral in the normal analysis scheme, actually decay with time when the full initial value treatment is considered.

At low mode numbers (usually $m = 2, 3, 4$ for the cases surveyed in this paper) the CC resonance is dominant over the CT interactions, yet the full-system growth rate is lower than expected due to the CC interaction alone. Thus the coupling to the external topographic perturbations causes stabilization of the system. At larger mode numbers the CT interaction becomes the only unstable one.

For a fixed radius of the upper layer ring R_1, the radius of the lower layer ring R_2 determines the type of resonance that leads to instability. When the lower ring is thin enough (i.e. R_2 is close to 1) the dominant resonance is CT; if $\Gamma_1 = +1$ (in which case the flow in both layers is clockwise) then it is specifically $\mathrm{C_2T}$, i.e. the lower ring contour resonates with the topographic perturbations existing outside it. If $\Gamma_1 = -1$ (in which case the flow in both layers is counterclockwise) then it is specifically $\mathrm{C_1T}$, i.e. the upper ring contour resonates with the topographic perturbations at $r > R_2$. The transition from small R_2 where the instability is $\mathrm{C_1T}$ (or $\mathrm{C_2T}$) to large R_2 where the instability is CC, occurs through the CCT instability. In this instability one of the perturbation types of the CC subsystem resonates with the topographic perturbations, but not C_1 (or C_2) itself.

The resonance of the contours with the topographic perturbations may be either dominated by barotropic or baroclinic couplings, which are easy to identify using the integral equation approach. Usually the barotropic couplings are dominant (the barotropic governor effect), but for a narrow region of the upper layer relative thickness λ_1, the dominant instability is of due to baroclinity. In this case the resonance of the contours is primarily with the asymptotic baroclinic topographic mode.

The nature of the instability reflects on the nonlinear evolution stage of the flow. In case of CC instability, the two contours change significantly during the phase-locking stage; this leads to modons formation and emission from the island. In CT instability the resonance is with a collection of topographic perturbation types having critical layers in proximity to one another. The result is a strengthening of the PV in a narrow ring at some distance at the lower layer. This ring interacts with the contours to form a quasi-stationary structure (e.g. a tripole); only at later times the structure breaks into modons which may be emitted from the island.

With some minor modifications, the beta-cone concept can be applied to the treatment of flows in the presence of conical beta effect in a planetary scale, namely, of the Antarctic Circumpolar Current. In this case the equation (2.2) for the upper layer PV is supplemented with an additional background planetary beta term $\beta_P r$ (related to the gradient of the Coriolis parameter), while β in the lower layer is replaced by $\beta_P + \beta_T$ (β_T being related to the bottom topography), see e.g. Kizner *et al.* (2017). In this case more resonances come into play, since more perturbation types are added in the upper layer. These issues will be considered separately elsewhere.

Acknowledgments

The author thanks Professor Z. Kizner for valuable discussions on this study. This research was supported by the US–Israel Science Foundation (BSF), Grant No. 2014206.

Appendix A. Velocity profile of the basic flow

Consider the basic flow, in which the PV in each of the layers is given by (4.1). The equations can be decoupled using the following definitions of the BT and BC modes of the basic flow (cf. Pedlosky 2013),

$$\bar{Q}_{BT} = \lambda_1\bar{Q}_1 + \lambda_2\bar{Q}_2, \quad \bar{\Psi}_{BT} = \lambda_1\bar{\Psi}_1 + \lambda_2\bar{\Psi}_2, \quad \beta_{BT} = \lambda_2\beta, \tag{A 1}$$

$$\bar{Q}_{BC} = \bar{Q}_1 - \bar{Q}_2, \quad \bar{\Psi}_{BC} = \bar{\Psi}_1 - \bar{\Psi}_2, \quad \beta_{BC} = -\beta. \tag{A 2}$$

From (A 1) and (A 2) we obtain

$$\bar{Q}_1 = \bar{Q}_{BT} + \lambda_2\bar{Q}_{BC}, \quad \bar{\Psi}_1 = \bar{\Psi}_{BT} + \lambda_2\bar{\Psi}_{BC}, \tag{A 3}$$

$$\bar{Q}_2 = \bar{Q}_{BT} - \lambda_1 \bar{Q}_{BC}, \quad \bar{\Psi}_2 = \bar{\Psi}_{BT} - \lambda_1 \bar{\Psi}_{BC}, \quad \beta_2 = \beta_{BT} - \lambda_1 \beta_{BC}. \tag{A 4}$$

Using (A 3) and (A 4) along with (2.4) we arrive at the equations that relate the modal PVs and streamfunctions,

$$\bar{Q}_{BT} = \nabla^2 \bar{\Psi}_{BT} + \beta_{BT} r, \tag{A 5}$$

$$\bar{Q}_{BC} = \nabla^2 \bar{\Psi}_{BT} - \tilde{\Lambda}^2 \bar{\Psi}_{BC} + \beta_{BC} r, \tag{A 6}$$

where $\tilde{\Lambda} = \Lambda/\sqrt{\lambda_1 \lambda_2}$. For definiteness, we assume that $R_2 > R_1$; otherwise the following expressions should be adapted in straightforward manner. Using (A 5) and (4.1), the barotropic streamfunction satisfies the equation

$$\bar{\Psi}''_{BT} + \frac{1}{r}\bar{\Psi}'_{BT} + \beta_{BT} r = \begin{cases} \lambda_1 \Gamma_1 + \lambda_2 \Gamma_2, & R \leqslant r \leqslant R_1 \\ \lambda_2 \Gamma_2, & R_1 < r \leqslant R_2 \\ \beta_{BT} r, & R_2 < r. \end{cases} \tag{A 7}$$

The general solution to (A 7) is

$$\bar{\Psi}_{BT} = \begin{cases} -\frac{1}{9}\beta_{BT} r^3 + \frac{1}{4}(\lambda_1 \Gamma_1 + \lambda_2 \Gamma_2) r^2 + C_1 \ln(r) + C_2, & R \leqslant r \leqslant R_1 \\ -\frac{1}{9}\beta_{BT} r^3 + \frac{1}{4}\lambda_2 \Gamma_2 r^2 + C_3 \ln(r) + C_4, & R_1 < r \leqslant R_2 \\ C_5 + C_6 \ln r, & R_2 < r. \end{cases} \tag{A 8}$$

It is known that the expression for the energy of the flow is (e.g. Solodoch *et al.* 2016)

$$E = \frac{1}{2}\iint_{r>R} [\lambda_1 (\nabla \bar{\Psi}_1)^2 + \lambda_2 (\nabla \bar{\Psi}_2)^2] r dr d\theta + \frac{1}{2}\Lambda^2 \iint_{r>R} (\Psi_1 - \Psi_2)^2 r dr d\theta, \tag{A 9}$$

in which the first integral represents the kinetic energy, and the second one, the available potential energy of the flow. The potential energy is associated with the baroclinic mode only, whereas the kinetic energy is contributed by both modes. Therefore, in order for the kinetic energy to be finite, the contribution to the first integral in (A 9) from the barotropic mode should be finite and we must set $C_6 = 0$ in (A 8). By (A 7) the barotropic streamfunction is continuous, as well as its first derivative, i.e.

$$\bar{\Psi}_{BT}(R_1^-) = \bar{\Psi}_{BT}(R_1^+), \quad \bar{\Psi}_{BT}(R_2^-) = \bar{\Psi}_{BT}(R_2^+), \tag{A 10}$$

$$\bar{\Psi}'_{BT}(R_1^+) = \bar{\Psi}'_{BT}(R_1^-), \quad \bar{\Psi}'_{BT}(R_2^+) = \bar{\Psi}'_{BT}(R_2^-). \tag{A 11}$$

From equations (A 10)-(A 11) the four unknowns $C_1 - C_4$ are found to be

$$C_1 = (1/3)\lambda_2 \beta R_2^3 - (1/2)\Gamma_1 R_1^2 \lambda_1 - (1/2)\lambda_2 \Gamma_2 R_2^2, \tag{A 12}$$

$$\begin{aligned} C_2 =& (1/2)\ln(R_1) R_1^2 \Gamma_1 \lambda_1 - (1/4) R_1^2 \Gamma_1 \lambda_1 - (1/3)\ln(R_2)\lambda_2 \beta R_2^3 \\ &+ (1/2)\ln(R_2)\lambda_2 \Gamma_2 R_2^2 + (1/9)\lambda_2 \beta R_2^3 - (1/4)\lambda_2 \Gamma_2 R_2^2 + C_5, \end{aligned} \tag{A 13}$$

$$C_3 = (1/3)\lambda_2 \beta R_2^3 - (1/2)\lambda_2 \Gamma_2 R_2^2, \tag{A 14}$$

$$\begin{aligned} C_4 =& -(1/3)\ln(R_2)\lambda_2 * beta R_2^3 + (1/2)\ln(R_2)\lambda_2 \Gamma_2 R_2^2 \\ &+ (1/9)\lambda_2 \beta R_2^3 - (1/4)\lambda_2 \Gamma_2 R_2^2 + C_5, \end{aligned} \tag{A 15}$$

The azimuthal barotropic velocity is, via (A 1)-(A 2) and (A 8),

$$\bar{V}_{BT} \equiv \frac{\partial \bar{\Psi}_{BT}}{\partial r} = \begin{cases} -\frac{1}{3}\beta_{BT} r^2 + \frac{1}{2}(\lambda_1 \Gamma_1 + \lambda_2 \Gamma_2) r + \frac{C_1}{r}, & R \leqslant r \leqslant R_1 \\ -\frac{1}{3}\lambda_2 \beta_2 r^2 + \frac{1}{2}\lambda_2 \Gamma_2 r + \frac{C_3}{r}, & R_1 < r \leqslant R_2 \\ 0, & R_2 < r. \end{cases} \tag{A 16}$$

The velocity is assumed to vanish at $r = R$, i.e. $\bar{V}_{BT}(R) = 0$ (see §4.1). Using (A 16) this imposes a relation between Γ_1 and Γ_2 which appears in (4.3). Due to Stokes theorem this is equivalent to the condition of vanishing the total barotropic excess PV (i.e. the PV resulting by omitting the background PV) in the two rings, $\int_R^{R_2} r\nabla^2\bar{\Psi}_{BT}dr = \lambda_1\int_R^{R_1} r\Gamma_1 dr + \lambda_2\int_R^{R_2} r(\Gamma_2-\beta r)dr = 0$.

Using (A 6) and (4.1), the baroclinic streamfunction satisfies the equation

$$\bar{\Psi}''_{BC} + \frac{1}{r}\bar{\Psi}'_{BC} - \tilde{\Lambda}^2\bar{\Psi}_{BC} + \beta_{BC}r = \begin{cases} \Gamma_1 - \Gamma_2, & R \leqslant r \leqslant R_1 \\ \beta_1 r - \Gamma_2, & R_1 < r \leqslant R_2 \\ \beta_{BC}r, & R_2 < r. \end{cases} \tag{A 17}$$

The general solution to (A 17) is

$$\bar{\Psi}_{BC} = \begin{cases} D_1K_0(\tilde{\Lambda}r) + D_2I_0(\tilde{\Lambda}r) - (\Gamma_1-\Gamma_2)/\tilde{\Lambda}^2 + is_{2,0}(i\tilde{\Lambda}r)\beta_{BC}/\tilde{\Lambda}^3, & R \leqslant r \leqslant R_1 \\ D_3K_0(\tilde{\Lambda}r) + D_4I_0(\tilde{\Lambda}r) + \Gamma_2/\tilde{\Lambda}^2 - is_{2,0}(i\tilde{\Lambda}r)\beta_2/\tilde{\Lambda}^3, & R_1 < r \leqslant R_2 \\ D_5K_0(\tilde{\Lambda}r) + D_6I_0(\tilde{\Lambda}r), & R_2 < r, \end{cases} \tag{A 18}$$

where $s_{2,0}$ is the Lommel function s of order $\{2,0\}$ (Watson 1995). For the energy (A 9) to be finite we must set $D_6 = 0$. The barotropic streamfunction satisfies the continuity conditions at $r = R_1$ and $r = R_2$, the continuity conditions of its derivative at these radii (the corresponding equations to (A 10) and (A 11 for the baroclinic mode) and its vanishing condition at $r = R$. By solving these five equations and using the relations

$$\frac{d}{dr}K_0(\tilde{\Lambda}r) = -\tilde{\Lambda}K_1(\tilde{\Lambda}r), \quad \frac{d}{dr}I_0(\tilde{\Lambda}r) = \tilde{\Lambda}I_1(\tilde{\Lambda}r), \quad \frac{d}{dr}s_{2,0}(i\tilde{\Lambda}r) = -\frac{1}{2}i\tilde{\Lambda}\pi L_1(\tilde{\Lambda}r), \tag{A 19}$$

(L_1 being the modified Struve function (Watson 1995)), the expressions for $D_1 - D_5$ can be found (not given here). The azimuthal baroclinic velocity is then

$$\bar{V}_{BC} \equiv \frac{\partial\bar{\Psi}_{BC}}{\partial r} = \begin{cases} -D_1\tilde{\Lambda}K_1(\tilde{\Lambda}r) + D_2\tilde{\Lambda}I_1(\tilde{\Lambda}r) + \pi L_1(\tilde{\Lambda}r)\beta_{BC}/\tilde{\Lambda}^2, & R \leqslant r \leqslant R_1 \\ -D_3\tilde{\Lambda}K_1(\tilde{\Lambda}r) + D_4\tilde{\Lambda}I_1(\tilde{\Lambda}r) - \pi L_1(\tilde{\Lambda}r)\beta_2/\tilde{\Lambda}^2, & R_1 < r \leqslant R_2 \\ -D_5\tilde{\Lambda}K_1(\tilde{\Lambda}r), & R_2 < r. \end{cases} \tag{A 20}$$

The basic velocity in each layer is then found by the equations

$$V_1 = V_{BT} + \lambda_2 V_{BC}, \quad V_2 = V_{BT} - \lambda_1 V_{BC}. \tag{A 21}$$

that follow from the above definitions (A 1)-(A 2), (A 16) and (A 20).

Appendix B. Barotropic and baroclinic Green functions

The barotropic Green function $G_{BT}(r,r')$ is defined by the equation

$$\frac{\mathrm{d}^2G_{BT}(r,r')}{\mathrm{d}r^2} + \frac{1}{r}\frac{\mathrm{d}G_{BT}(r,r')}{\mathrm{d}r} - \frac{m^2}{r^2}G_{BT}(r,r') = \delta(r-r'), \tag{B 1}$$

and satisfies the boundary conditions

$$G_{BT}(r=R,r') = 0, \quad G_{BT}(r\to\infty,r') = 0. \tag{B 2}$$

The general solution to (B 1) is

$$G_{BT} = \begin{cases} ar^m + br^{-m} & R \leqslant r < r', \\ cr^m + dr^{-m} & r' < r. \end{cases} \tag{B 3}$$

Imposing the boundary conditions (B 2) we get $b = -aR^{2m}$ and $c = 0$. By (B 1) the Green function is continuous at $r = r'$,

$$G_{BT}(r'^{+}, r') = G_{BT}(r'^{-}, r'). \tag{B 4}$$

Integration of (B 1) in the neighborhoods of the singularity $r = r'$ yields

$$G_{BT}(r'^{+}, r') - G_{BT}(r'^{-}, r') = 1. \tag{B 5}$$

Using (B 4) and (B 5) the coefficients a, b and d in (B 3) are found; the solution is

$$G_{BT}(r, r') = \begin{cases} \frac{r'^{-m+1}}{2m}\left(R^{2m} r^{-m} - r^{m}\right) & R \leqslant r \leqslant r', \\ \frac{r'^{-m+1}(R^{2m} - r'^{2m})}{2m} r^{-m} & r' < r. \end{cases} \tag{B 6}$$

In the same manner, the baroclinic Green function G_{BC} is defined by the equation

$$\frac{\mathrm{d}^2 G_{BC}(r, r')}{\mathrm{d}r^2} + \frac{1}{r}\frac{\mathrm{d}G_{BC}(r, r')}{\mathrm{d}r} - \frac{m^2}{r^2} G_{BC}(r, r') - \frac{\Lambda^2}{\lambda_1 \lambda_2} G_{BC}(r, r') = \delta(r - r'), \tag{B 7}$$

and satisfies the boundary conditions

$$G_{BC}(r = R, r') = 0, \quad G_{BC}(r \to \infty, r') = 0. \tag{B 8}$$

The general solution to (B 7) is (denoting $\tilde{\Lambda} = \Lambda/\sqrt{\lambda_1 \lambda_2}$)

$$G_{BC}^{m} = \begin{cases} \tilde{a} K_m(\tilde{\Lambda} r) + \tilde{b} I_m(\tilde{\Lambda} r) & R \leqslant r \leqslant r', \\ \tilde{c} K_m(\tilde{\Lambda} r) + \tilde{d} I_m(\tilde{\Lambda} r) & r' < r. \end{cases} \tag{B 9}$$

Imposing the boundary conditions (B 8) we get $\tilde{b} = -\tilde{a} K_m(\tilde{\Lambda} R)/I_m(\tilde{\Lambda} R)$ and $\tilde{d} = 0$. By (B 7) the Green function is continuous at $r = r'$,

$$G_{BC}(r'^{+}, r') = G_{BC}(r'^{-}, r'). \tag{B 10}$$

Integration of (B 7) in the neighborhoods of the singularity $r = r'$ yields

$$G_{BC}(r'^{+}, r') - G_{BC}(r'^{-}, r') = 1. \tag{B 11}$$

Using (B 10) and (B 11) and the identity $I_m K_{m+1} + I_{m+1} K_m = 1/r$ (Abramowitz & Stegun 1964) we get the solution

$$G_{BC}(r, r') = \begin{cases} r'\left(I_m(\tilde{\Lambda} R) K_m(\tilde{\Lambda} r) - I_m(\tilde{\Lambda} r) K_m(\tilde{\Lambda} R)\right) \frac{K_m(\tilde{\Lambda} r')}{\tilde{\Lambda} K_m(\tilde{\Lambda} R)} & R \leqslant r \leqslant r', \\ r'\left(I_m(\tilde{\Lambda} R) K_m(\tilde{\Lambda} r') - I_m(\tilde{\Lambda} r') K_m(\tilde{\Lambda} R)\right) \frac{K_m(\tilde{\Lambda} r)}{\tilde{\Lambda} K_m(\tilde{\Lambda} R)} & r' < r. \end{cases} \tag{B 12}$$

We note that both $\frac{G_{BT}(r,r')}{r'}$ and $\frac{G_{BC}(r,r')}{r'}$ are symmetric with respect to switching of the variables r and r'; this fact is used in §6.

Appendix C. Pseudomomentum continuity equation

Substituting (4.6) in (3.2) gives

$$\frac{\partial s_1}{\partial t} + \frac{\bar{V}_1}{r}\frac{\partial s_1}{\partial \theta} + \frac{1}{r}\frac{\partial \psi_1}{\partial \theta} = 0, \quad \frac{\partial s_2}{\partial t} + \frac{\bar{V}_2}{r}\frac{\partial s_2}{\partial \theta} + \frac{1}{r}\frac{\partial \psi_2}{\partial \theta} = 0. \tag{C 1}$$

Multiplying both equations of (C 1) by $s_i \frac{dQ_i}{dr}$ and integrating azimuthally we get

$$\frac{1}{2}\frac{d\bar{Q}_1}{dr}\frac{\partial}{\partial t}\int_0^{2\pi} s_1^2 d\theta + \frac{1}{2}\frac{d\bar{Q}_1}{dr}\frac{\bar{V}_1}{r}\int_0^{2\pi}\frac{\partial s_1^2}{\partial \theta} d\theta - \frac{1}{r}\int_0^{2\pi} q_1 \frac{\partial \psi_1}{\partial \theta} d\theta = 0 \tag{C 2}$$

$$\frac{1}{2}\frac{d\bar{Q}_2}{dr}\frac{\partial}{\partial t}\int_0^{2\pi} s_2^2\, d\theta + \frac{1}{2}\frac{d\bar{Q}_2}{dr}\frac{\bar{V}_2}{r}\int_0^{2\pi}\frac{\partial s_2^2}{\partial \theta}d\theta - \frac{1}{r}\int_0^{2\pi} q_2\frac{\partial \psi_2}{\partial \theta}d\theta = 0 \tag{C 3}$$

The second integrals in (C 2) and (C 3) vanish identically. Multiplying (C 2) by λ_1 and (C 3) by λ_2 and adding gives

$$\frac{1}{2}\frac{\partial}{\partial t}\int_0^{2\pi}\left(\lambda_1 r\frac{dQ_1}{dr}s_1^2 + \lambda_2 r\frac{dQ_2}{dr}s_2^2\right)d\theta = \int_0^{2\pi}\left(\lambda_1 q_1\frac{\partial \psi_1}{\partial \theta} + \lambda_2 q_2\frac{\partial \psi_2}{\partial \theta}\right)d\theta. \tag{C 4}$$

Since $q_1 = \nabla^2\psi_1 - \frac{\Lambda^2}{\lambda_1}(\psi_1 - \psi_2)$ and $q_2 = \nabla^2\psi_2 + \frac{\Lambda^2}{\lambda_2}(\psi_1 - \psi_2)$ (by (2.4)) the RHS of (C 4) turns to (some of the integrals vanish identically),

$$\int_0^{2\pi}\left(\lambda_1\nabla^2\psi_1\frac{\partial \psi_1}{\partial \theta} + \lambda_2\nabla^2\psi_2\frac{\partial \psi_2}{\partial \theta}\right)d\theta. \tag{C 5}$$

The first term in the integral may be written as

$$\nabla^2\psi_1\frac{\partial \psi_1}{\partial \theta} = \frac{1}{r}\frac{\partial}{\partial r}\left(r\frac{\partial \psi_1}{\partial \theta}\frac{\partial \psi_1}{\partial r}\right) - \frac{1}{2}\frac{\partial}{\partial \theta}\left(\frac{\partial \psi_1}{\partial r}\frac{\partial \psi_1}{\partial r}\right) + \frac{1}{2r^2}\frac{\partial}{\partial \theta}\left(\frac{\partial \psi_1}{\partial \theta}\frac{\partial \psi_1}{\partial \theta}\right), \tag{C 6}$$

and upon substitution of (C 6) in (C 4) we get

$$-\frac{1}{2}\frac{\partial}{\partial t}\int_0^{2\pi}\left(\lambda_1 r\frac{dQ_1}{dr}s_1^2 + \lambda_2 r\frac{dQ_2}{dr}s_2^2\right)d\theta + \frac{1}{r}\frac{\partial}{\partial r}\int_0^{2\pi}\left(\lambda_1\frac{\partial \psi_1}{\partial \theta}\frac{\partial \psi_1}{\partial r} + \lambda_2\frac{\partial \psi_2}{\partial \theta}\frac{\partial \psi_2}{\partial r}\right)d\theta. \tag{C 7}$$

This is the continuity equation for the pseudomomentum appearing in (5.2).

Appendix D. The differential equation for the topographic perturbations at $r > R_2$

Define the operators

$$\mathrm{D}_1 = \partial_r^2 + \frac{1}{r}\partial_r - \frac{m^2}{r^2}, \quad \mathrm{D}_2 = \partial_r^2 + \frac{1}{r}\partial_r - \frac{m^2}{r^2} - \frac{\Lambda^2}{\lambda_1\lambda_2}, \tag{D 1}$$

which, according to the definitions of the barotropic and baroclinic Green functions (see Appendix B) satisfy

$$\mathrm{D}_1 G_{BT}(r,r') = \delta(r-r'), \quad \mathrm{D}_2 G_{BC}(r,r') = \delta(r-r'). \tag{D 2}$$

Define also

$$\mathrm{D}_3 = \partial_r^2 - \frac{1}{r}\partial_r - \frac{m^2}{r^2}, \quad \mathrm{D}_4 = \partial_r^2 - \frac{1}{r}\partial_r - \frac{m^2}{r^2} - \frac{\Lambda^2}{\lambda_1\lambda_2}. \tag{D 3}$$

By imposing the operator $\mathrm{D}_1\mathrm{D}_2$ on both sides of (6.9), using (3.18) and the identity

$$\int_{R_2}^{\infty}\delta^{(k)}(r)f(r)dr = (-1)^k\int_{R_2}^{\infty}\delta(r)f^{(k)}(r)dr, \tag{D 4}$$

a fourth-order non-homogeneous differential equation is achieved,

$$\begin{aligned}\mathrm{D}_1\mathrm{D}_2\xi(r) = &-\frac{\mathrm{D}_1\mathrm{D}_2 G_{22}(r,r_c)}{r_c}\\ &+\beta\lambda_2\mathrm{D}_4\left[\frac{1/r - 1/r_c}{\frac{\bar{V}_2(r)}{r} - \frac{\omega}{m}}\xi(r)\right] + \beta\lambda_1\mathrm{D}_3\left[\frac{1/r - 1/r_c}{\frac{\bar{V}_2(r)}{r} - \frac{\omega}{m}}\xi(r)\right],\end{aligned} \tag{D 5}$$

where the source term is proportional to $\delta(r-r_c)$ and its derivatives,

$$\begin{aligned}\mathrm{D}_1\mathrm{D}_2G_{22}(r,r_c) &= \mathrm{D}_2\mathrm{D}_1\lambda_2G_{BT}(r,r_c)+\mathrm{D}_1\mathrm{D}_1\lambda_1G_{BC}(r,r_c)\\ &= \lambda_2\mathrm{D}_2\delta(r-r_c)+\lambda_1\mathrm{D}_1\delta(r-r_c)\\ &= \mathrm{D}_1\delta(r-r_c)-\frac{\mathit{\Lambda}^2}{\lambda_1}\delta(r-r_c)\\ &= \delta''(r-r_c)+\frac{\delta'(r-r_c)}{r}-\left(\frac{m^2}{r^2}+\frac{\mathit{\Lambda}^2}{\lambda_1}\right)\delta(r-r_c).\end{aligned} \tag{D 6}$$

Appendix E. Poles of the response function

In this appendix the types of poles of the response function $\chi(r;r_9,\omega)$ defined by (6.30) are determined. By (6.30), for any $\omega\neq m\bar{V}_2(r_0)/r_0$, χ can be written as

$$\chi(r;r_0,\omega)=\frac{1}{\frac{\bar{V}_2(r_0)}{r_0}-\frac{\omega}{m}}\delta(r-r_0)+X(r;r_0,\omega), \tag{E 1}$$

where $X(r,r_0;\omega)$ satisfies the following equation,

$$\left(\frac{\bar{V}_2}{r}-\frac{\omega}{m}\right)X(r;r_0,\omega)-\beta\int_{R_2}^{\infty}\frac{G_{22}(r,r')}{r'}X(r';r_0,\omega)dr'=\beta\frac{G_{22}(r,r_0)}{\frac{\bar{V}_2(r_0)}{r_0}-\frac{\omega r_0}{m}}. \tag{E 2}$$

By (E 1), at $\omega=m\bar{V}_2(r_0)/r_0$ there is a pole. Equation (E 2) is singular at $r=r_c=(m\bar{V}_2/r)^{-1}(\omega)$ and so the same ansatz as in (6.1) is used,

$$X(r;r_0,\omega)=D(r_0,\omega)\delta\left(\frac{\bar{V}_2}{r}-\frac{\omega}{m}\right)-\frac{\beta}{\frac{\bar{V}_2}{r}-\frac{\omega}{m}}\xi(r;r_0,\omega). \tag{E 3}$$

where now the last term is defined not via the principal value, and ξ is assumed to be a regular function of r. Substitution of (E 3) in (E 2) results in the following equation,

$$-\xi(r;r_0,\omega)-\frac{D(r_0,\omega)G_{22}(r,r_c)}{|(V(r)/r)'_{r_c}|r_c}+\int_{R_2}^{\infty}\frac{\beta G_{22}(r,r')}{(\frac{\bar{V}_2(r')}{r'}-\frac{\omega}{m})r'}\xi(r';r_0,\omega)dr'=\frac{G_{22}(r,r_0)}{\frac{\bar{V}_2(r_0)}{r_0}-\frac{\omega r_0}{m}}. \tag{E 4}$$

By substituting $r=R$ in (E 4), the function $D(r_0,\omega)$ can be expressed in terms of ξ,

$$D(r_0,\omega)=\frac{|(V(r)/r)'_{r_c}|r_c}{G_{22}(R,r_c)}\left[\xi(R;r_0,\omega)-\int_{R_2}^{\infty}\frac{\beta G_{22}(R,r')}{(\frac{\bar{V}_2(r')}{r'}-\frac{\omega}{m})r'}\xi(r';r_0,\omega)dr'-\frac{G_{22}(R,r_0)}{\frac{\bar{V}_2(r_0)}{r_0}-\frac{\omega r_0}{m}}\right]. \tag{E 5}$$

By (E 5), $D(r_0,\omega)$ has poles along the entire segment $\mathcal{S}_1$ as well as the poles of $\xi(r;r_0,\omega)$. The poles of $\xi(r;r_0,\omega)$ appear also in the second term in the RHS of (E 3).

Another class of singularities appear upon solving (E 2) for $\omega\notin\mathcal{S}_1$. Imposing the operator $\mathrm{D}_1\mathrm{D}_2$ (where D_1 and D_2 are defined by (D 1)) on both sides of (E 2), and using (D 2) and (D 6), results in the following equation,

$$\begin{aligned}&\mathrm{D}_1\mathrm{D}_2[\left(\frac{\bar{V}_2}{r}-\frac{\omega}{m}\right)X(r,r_0;\omega)]-\frac{\beta\mathrm{D}_2X(r,r_0;\omega)}{r}=\\ &\qquad\beta\frac{\delta''(r-r_0)+\delta(r-r_0)/r_0-(m^2/r^2+\mathit{\Lambda}^2/\lambda_2)\delta(r-r_0))}{\frac{\bar{V}_2(r_0)}{r_0}-\frac{\omega r_0}{m}}.\end{aligned} \tag{E 6}$$

The solution to (E 6) can be found in the following way: first, we solve the homogeneous part and find four linearly independent solutions. Then, in any of the region $R_2 < r < r_0$ and $r_0 < r$, the solution is written as a linear combination of the four solutions with totally 8 constant coefficients (4 for each region). In the asymptotic limit $r \gg r_0$, equation (E 2) is the same as (6.1), and therefore only two solutions exist (i.e. the asymptotically BT and BC solutions, see §4.2). This leaves us with 6 constant coefficients. There are two boundary conditions that can be found at $r = R_2$ by applying (E 2) and its derivative at $r = R_2$, and 4 equations that match the solutions and their derivatives (up to the third order derivative) on both sides of $r = r_0$; the matching conditions are determined from the delta-terms in the RHS of (E 6). So, there are six (non-homogeneous) equations for the six unknown coefficients that we designate as $A_1, A_2, ...A_6$. The equations can be recast to a standard matrix notation $\mathrm{M}(r_0, \omega)\mathbf{a} = \mathbf{b}$, where $\mathbf{a} = (A_1, ..., A_6)$ and $\mathbf{b} \neq \mathbf{0}$. By Cramer's rule the solutions are $A_i = \frac{\det(M_i(r_0,\omega))}{\det(M(r_0,\omega))}$, where $M_i(r_0, \omega)$ signifies the matrix formed by replacing the i-th column of M by the column vector $\mathbf{b}$. Therefore $X(r; r_0, \omega)$ is non-analytic when the joint denominator of the coefficients, $\det(M(r_0, \omega))$, is zero. Since the determinant is a continuous function of ω, its zeros constitute a discrete set of points.

Appendix F. Sign of pseudomomentum via slope of dispersion curves

The proof here closely follows that of Iga (1999*a*), that was done for one-layer shallow water system. Since Rayleigh equation (3.4) is well defined for any $m > 0$ (not necessarily an integer) here we treat m as a continuous variable, although in practice it must be an integer (see equation (3.3)). Multiply Rayleigh equation (3.4) by the complex conjugate of another solution $\mathcal{Q}_1$ corresponding to a different mode number $\tilde{m}$,

$$\left(\frac{\bar{V}_1(r)}{r} - \frac{\omega}{m}\right)\mathcal{Q}_1\tilde{\mathcal{Q}}_1^* - \frac{\varPhi_1}{r}\frac{d\bar{Q}_1}{dr}\tilde{\mathcal{Q}}_1^* = 0. \tag{F 1}$$

Multiply Rayleigh equation (3.4) for the other solution by the complex conjugate of the first solution, and conjugate the result

$$\left(\frac{\bar{V}_1(r)}{r} - \frac{\tilde{\omega}^*}{\tilde{m}}\right)\tilde{\mathcal{Q}}_1^*\mathcal{Q}_1 - \frac{\tilde{\varPhi}_1}{r}\frac{d\bar{Q}_1}{dr}\mathcal{Q}_1 = 0. \tag{F 2}$$

If the perturbation is stable then $\tilde{\omega}^* = \tilde{\omega}$. Subtracting the two equations gives

$$\left(\frac{\tilde{\omega}}{\tilde{m}} - \frac{\omega}{m}\right)\mathcal{Q}_1\tilde{\mathcal{Q}}_1^* - \frac{1}{r}\frac{d\bar{Q}_1}{dr}(\varPhi_1\tilde{\mathcal{Q}}_1^* - \tilde{\varPhi}_1^*\mathcal{Q}_1) = 0. \tag{F 3}$$

$$\begin{aligned}\left(\frac{\tilde{\omega}}{\tilde{m}} - \frac{\omega}{m}\right)\mathcal{Q}_1\tilde{\mathcal{Q}}_1^* = {}& \frac{1}{r}\frac{d\bar{Q}_1}{dr}\left(\varPhi_1\frac{d^2\tilde{\varPhi}_1^*}{dr^2} + \frac{\varPhi_1}{r}\frac{d\tilde{\varPhi}_1^*}{dr} - \frac{\tilde{m}^2}{r^2}\varPhi_1\tilde{\varPhi}_1^* - \frac{\varLambda^2}{\lambda_1}\varPhi_1(\tilde{\varPhi}_1^* - \tilde{\varPhi}_2^*)\right)\\ & - \frac{1}{r}\frac{d\bar{Q}_1}{dr}\left(\varPhi_1\frac{d^2\tilde{\varPhi}_1^*}{dr^2} + \frac{\tilde{\varPhi}_1^*}{r}\frac{d\varPhi_1}{dr} - \frac{m^2}{r^2}\tilde{\varPhi}_1^*\varPhi_1 - \frac{\varLambda^2}{\lambda_1}\tilde{\varPhi}_1^*(\varPhi_1 - \varPhi_2)\right).\end{aligned} \tag{F 4}$$

Similar equations can be written for the second layer,

$$\begin{aligned}\left(\frac{\tilde{\omega}}{\tilde{m}} - \frac{\omega}{m}\right)\mathcal{Q}_2\tilde{\mathcal{Q}}_2^* = {}& \frac{1}{r}\frac{d\bar{Q}_2}{dr}\left(\varPhi_2\frac{d^2\tilde{\varPhi}_2^*}{dr^2} + \frac{\varPhi_2}{r}\frac{d\tilde{\varPhi}_2^*}{dr} - \frac{\tilde{m}^2}{r^2}\varPhi_2\tilde{\varPhi}_2^* + \frac{\varLambda^2}{\lambda_2}\varPhi_2(\tilde{\varPhi}_2^* - \tilde{\varPhi}_1^*)\right)\\ & - \frac{1}{r}\frac{d\bar{Q}_1}{dr}\left(\varPhi_2\frac{d^2\tilde{\varPhi}_2^*}{dr^2} + \frac{\tilde{\varPhi}_2^*}{r}\frac{d\varPhi_2}{dr} - \frac{m^2}{r^2}\tilde{\varPhi}_2^*\varPhi_2 + \frac{\varLambda^2}{\lambda_2}\tilde{\varPhi}_2^*(\varPhi_2 - \varPhi_1)\right).\end{aligned} \tag{F 5}$$

Multiplying (F 4) by $r\lambda_1$ and (F 5) by $r\lambda_2$, adding, and then integrating with respect to r gives, after taking the limit $m \to \tilde{m}$,

$$\frac{d(\omega/m)}{dm}\int_R^\infty r\left(\lambda_1\frac{d\bar{Q}_1}{dr}|d_1|^2+\lambda_2\frac{d\bar{Q}_2}{dr}|d_2|^2\right)dr=-\frac{2m}{r^3}\int_R^\infty \lambda_1|\varPhi_1|^2+\lambda_2|\varPhi_2|^2 dr. \quad \text{(F 6)}$$

Using the definition of the pseudomomentum (5.1) we get

$$\frac{d(\omega/m)}{dm}M=\frac{2m}{r^3}\int_R^\infty \lambda_1|\varPhi_1|^2+\lambda_2|\varPhi_2|^2 dr. \quad \text{(F 7)}$$

The right hand side is always positive, so M has the same sign as $d(\omega/m)/dm$.

Appendix G. Rewriting the eigenvalue equation in terms of the CC modes

The two CC perturbations types are denoted by A and B; each type corresponds to different perturbations of the contours α_1 and α_2 and frequency. We write the perturbations in vector form for ease of notation, so the eigenvectors of the CC system are

$$\begin{bmatrix}\alpha_1\\ \alpha_2\end{bmatrix}_A=\begin{bmatrix}\alpha_{1A}\\ \alpha_{2A}\end{bmatrix},\quad \begin{bmatrix}\alpha_1\\ \alpha_2\end{bmatrix}_B=\begin{bmatrix}\alpha_{1B}\\ \alpha_{2B}\end{bmatrix}, \quad \text{(G 1)}$$

with eigenvalues ω_a and ω_b respectively. A general perturbation of the contours of the full system can be written as

$$\begin{bmatrix}\alpha_1\\ \alpha_2\end{bmatrix}=a\begin{bmatrix}\alpha_{1A}\\ \alpha_{2A}\end{bmatrix}+b\begin{bmatrix}\alpha_{1B}\\ \alpha_{2B}\end{bmatrix}. \quad \text{(G 2)}$$

Plugging (G 2) into (4.9) and (4.10) and using the fact that the vectors in (G 1) are the CC eigenvectors we get

$$\frac{\omega_a}{m}\alpha_{1A}a+\frac{\omega_b}{m}\alpha_{1B}b-\beta\varDelta_1\int_{R_2}^\infty \frac{G_{12}(R_1,r')}{r'}\eta(r')dr'=\frac{\omega}{m}(a\alpha_{1A}+b\alpha_{1B}) \quad \text{(G 3)}$$

$$\frac{\omega_a}{m}\alpha_{2A}a+\frac{\omega_b}{m}\alpha_{2B}b-\beta\varDelta_2\int_{R_2}^\infty \frac{G_{22}(R_2,r')}{r'}\eta(r')dr'=\frac{\omega}{m}(a\alpha_{2A}+b\alpha_{2B}). \quad \text{(G 4)}$$

Multiplying (G 3) by α_{2B} and (G 4) by α_{1B} and subtracting we get

$$\begin{aligned}\frac{\omega_a}{m}(\alpha_{1A}\alpha_{2B}-\alpha_{2A}\alpha_{1B})a-\beta\varDelta_1\alpha_{2B}\int_{R_2}^\infty \frac{G_{12}(R_1,r')}{r'}\eta(r')dr'\\ +\beta\varDelta_2\alpha_{1B}\int_{R_2}^\infty \frac{G_{22}(R_2,r')}{r'}\eta(r')dr'=\frac{\omega}{m}(\alpha_{1A}\alpha_{2B}-\alpha_{2A}\alpha_{1B})a\end{aligned} \quad \text{(G 5)}$$

Multiplying (G 3) by α_{2A} and (G 4) by α_{1A} and subtracting we get

$$\begin{aligned}\frac{\omega_b}{m}(\alpha_{2A}\alpha_{1B}-\alpha_{1A}\alpha_{2B})b-\beta\varDelta_1\alpha_{2A}\int_{R_2}^\infty \frac{G_{12}(R_1,r')}{r'}\eta(r')dr'\\ +\beta\varDelta_2\alpha_{1A}\int_{R_2}^\infty \frac{G_{22}(R_2,r')}{r'}\eta(r')dr'=\frac{\omega}{m}(\alpha_{2A}\alpha_{1B}-\alpha_{1A}\alpha_{2B})b\end{aligned} \quad \text{(G 6)}$$

The third equation results from substituting (G 2) in (4.11),

$$-\frac{G_{21}(r,R_1)}{R_1}(a\alpha_{1A}+b\alpha_{1B})-\frac{G_{22}(r,R_2)}{R_2}(a\alpha_{2A}+b\alpha_{2B})+\frac{\bar{V}_2(r)}{r}\eta(r) \\ -\beta\int_{R_2}^{\infty}\frac{G_{22}(r,r')}{r'}\eta(r')dr'=\frac{\omega}{m}\eta(r). \qquad \text{(G 7)}$$

REFERENCES

ABRAMOWITZ, M. & STEGUN, I.A. 1964 *Handbook of mathematical functions: with formulas, graphs, and mathematical tables*. Courier Corporation.

ADAM, J.A. 1986 Critical layer singularities and complex eigenvalues in some differential equations of mathematical physics. *Phys. Rep.* **142** (5), 263–356.

BATEMAN, HARRY 1954 *Tables of integral transforms [volume I]*, , vol. 1. McGraw-Hill Book Company.

BRETHERTON, FRANCIS P 1966 Critical layer instability in baroclinic flows. *Quarterly Journal of the Royal Meteorological Society* **92** (393), 325–334.

BRIGGS, RJ, DAUGHERTY, JD & LEVY, RH 1970 Role of landau damping in crossed-field electron beams and inviscid shear flow. *The Physics of Fluids* **13** (2), 421–432.

BRINK, K.H. 1999 Island-trapped waves, with application to observations off bermuda. *Dyn. Atmos. Oceans* **29** (2), 93–118.

BURGER, ALLWYN 1966 Instability associated with the continuous spectrum in a baroclinic flow. *Journal of the Atmospheric Sciences* **23** (3), 272–277.

CAIRNS, RA 1979 The role of negative energy waves in some instabilities of parallel flows. *Journal of Fluid Mechanics* **92** (1), 1–14.

CASE, KM 1960 Stability of inviscid plane couette flow. *The Physics of Fluids* **3** (2), 143–148.

CHOPRA, KULDIP P 1973 Atmospheric and oceanic flow problems introduced by islands. In *Advances in Geophysics*, , vol. 16, pp. 297–421. Elsevier.

CORREAD, SM & CARTON, XJ 1999 Formation and stability of tri-polar vortices in stratified geostrophic flows. *Nuovo Cimento. C* **22** (6), 767–777.

DYKE, PHIL 2005 Wave trapping and flow around an irregular near circular island in a stratified sea. *Ocean Dyn.* **55** (3-4), 238–247.

FLIERL, G.R. 1988 On the instability of geostrophic vortices. *J. Fluid Mech.* **197**, 349–388.

FLIERL, GR, LARICHEV, VD, MCWILLIAMS, JC & REZNIK, GM 1980 The dynamics of baroclinic and barotropic solitary eddies. *Dynamics of Atmospheres and Oceans* **5** (1), 1–41.

HAYASHI, Y-Y & YOUNG, WR 1987 Stable and unstable shear modes of rotating parallel flows in shallow water. *Journal of Fluid Mechanics* **184**, 477–504.

HEIFETZ, E., BISHOP, C.H. & ALPERT, P. 1999 Counter-propagating rossby waves in the barotropic rayleigh model of shear instability. *Quart. J. Roy. Meteor. Soc.* **125** (560), 2835–2853.

HILDEBRAND, FRANCIS BEGNAUD 1987 *Introduction to numerical analysis*. Courier Corporation.

HOURY, S., DOMBROWSKY, E., P., DE MEY & M., JEAN-FRANCOIS 1987 Brunt-väisälä frequency and rossby radii in the south atlantic. *J. Phys. Oceanogr.* **17** (10), 1619–1626.

IGA, KEITA 1997 Instability of a front with a layer of uniform potential vorticity. *Journal of the Meteorological Society of Japan. Ser. II* **75** (1), 1–11.

IGA, KEITA 1999*a* Critical layer instability as a resonance between a non-singular mode and continuous modes. *Fluid dynamics research* **25** (2), 63–86.

IGA, KEITA 1999*b* A simple criterion for the sign of the pseudomomentum of modes in shallow water systems. *Journal of Fluid Mechanics* **387**, 343–352.

JAMES, IN 1987 Suppression of baroclinic instability in horizontally sheared flows. *Journal of the atmospheric sciences* **44** (24), 3710–3720.

JONES, WALTER L 1967 Propagation of internal gravity waves in fluids with shear flow and rotation. *Journal of Fluid Mechanics* **30** (3), 439–448.

KAMP, LPJ 1991 Integral-equation approach to the instability of two-dimensional sheared flow of inviscid fluid in a rotating system with variable coriolis parameter. *Journal of Physics A: Mathematical and General* **24** (9), 2029.

Killingbeck, J 2012 *Mathematical techniques and physical applications*, , vol. 35. Elsevier.

Kizner, ZI 1984 Rossby solitons with axisymmetric baroclinic modes. In *Dokl. Akad. Nauk SSSR*, , vol. 275, pp. 1495–1498.

Kizner, Z 1997 Solitary rossby waves with baroclinic modes. *Journal of marine research* **55** (4), 671–685.

Kizner, Z., Makarov, V., Kamp, L. & van Heijst, G.J.F. 2013 Instabilities of the flow around a cylinder and emission of vortex dipoles. *J. Fluid Mech.* **730**, 419–441.

Kizner, Z., Shteinbuch-Fridman, B., Makarov, V. & Rabinovich, M. 2017 Cycloidal meandering of a mesoscale anticyclonic eddy. *Phys. Fluids* **29** (8), 086601.

Kowalik, Z. & Stabeno, P. 1999 Trapped motion around the pribilof islands in the bering sea. *J. Geoph. Res.: Oceans* **104** (C11), 25667–25684.

Kubokawa, Atsushi 1986 Instability caused by the coalescence of two modes of a one-layer coastal current with a surface front. *Journal of Oceanography* **42** (5), 373–380.

Lin, Chia-Chiao 1945 On the stability of two-dimensional parallel flows. i. general theory. *Quarterly of Applied Mathematics* **3** (2), 117–142.

Longuet-Higgins, M.S. 1967 On the trapping of wave energy round islands. *J. Fluid Mec.* **29** (4), 781–821.

Longuet-Higgins, M.S. 1969 On the trapping of long-period waves round islands. *J. Fluid Mech.* **37** (04), 773–784.

Mechoso, Carlos R 1980 Baroclinic instability of flows along sloping boundaries. *Journal of the Atmospheric Sciences* **37** (6), 1393–1399.

Mihanović, Hrvoje, Paklar, Gordana Beg & Orlić, Mirko 2014 Resonant excitation of island-trapped waves in a shallow, seasonally stratified sea. *Continental Shelf Research* **77**, 24–37.

Moler, Cleve B & Stewart, Gilbert W 1973 An algorithm for generalized matrix eigenvalue problems. *SIAM Journal on Numerical Analysis* **10** (2), 241–256.

Pedlosky, Joseph 1964 The stability of currents in the atmosphere and the ocean: Part i. *Journal of the Atmospheric Sciences* **21** (2), 201–219.

Pedlosky, J. 2013 *Geophysical fluid dynamics*. Springer Science & Business Media.

Phillips, Norman A 1951 A simple three-dimensional model for the study of large-scale extratropical flow patterns. *Journal of Meteorology* **8** (6), 381–394.

Rabinovich, M., Kizner, Z. & Flierl, G. 2018 Bottom-topography effect on the instability of flows around a circular island. *J. Fluid Mech.* **856**, 202–227.

Rabinovich, Michael, Kizner, Ziv & Flierl, Glenn 2019 Barotropic annular flows, vortices and waves on a beta cone. *Journal of Fluid Mechanics* **875**, 225–253.

Ribstein, Bruno & Zeitlin, Vladimir 2013 Instabilities of coupled density fronts and their nonlinear evolution in the two-layer rotating shallow-water model: influence of the lower layer and of the topography. *Journal of Fluid Mechanics* **716**, 528–565.

Riedinger, Xavier & Gilbert, Andrew D 2014 Critical layer and radiative instabilities in shallow-water shear flows. *Journal of Fluid Mechanics* **751**, 539–569.

Riedinger, Xavier, Meunier, Patrice & Le Dizes, Stéphane 2010 Instability of a vertical columnar vortex in a stratified fluid. *Experiments in fluids* **49** (3), 673–681.

Sakai, Satoshi 1989 Rossby-kelvin instability: a new type of ageostrophic instability caused by a resonance between rossby waves and gravity waves. *Journal of Fluid Mechanics* **202**, 149–176.

Satomura, Takehiko 1981 An investigation of shear instability in a shallow water. *Journal of the Meteorological Society of Japan. Ser. II* **59** (1), 148–167.

Shtokman, V.B. 1966 A qualitative analysis of the causes of the anomalous circulation around oceanic islands. *Izv. Atmos. Oceanic Phys.)* **2**, 723–728.

Sokolovskiy, MA & Verron, J 2000 Finite-core hetons: stability and interactions. *Journal of Fluid Mechanics* **423**, 127–154.

Solodoch, Aviv, Stewart, Andrew L & McWilliams, James C 2016 Baroclinic instability of axially symmetric flow over sloping bathymetry. *Journal of Fluid Mechanics* **799**, 265–296.

Vallis, G.K. 2017 *Atmospheric and oceanic fluid dynamics*. Cambridge University Press.

Van Kampen, Nicolaas G 1955 On the theory of stationary waves in plasmas. *Physica* **21** (6-10), 949–963.

Watson, G. N. 1995 *A treatise on the theory of Bessel functions*. Cambridge university press.

Whittaker, Edmund Taylor & Watson, George Neville 1996 *A course of modern analysis*. Cambridge university press.

Wimp, Jet 1965 On the zeros of a confluent hypergeometric function. *Proceedings of the American Mathematical Society* **16** (2), 281–283.

Wunsch, Carl 1972 The spectrum from two years to two minutes of temperature fluctuations in the main thermocline at bermuda. In *Deep Sea Research and Oceanographic Abstracts*, , vol. 19, pp. 577–593. Elsevier.